Estimating 13.8-GHz Path-Integrated Attenuation from 10.7-GHz Brightness Temperatures for the TRMM Combined PR–TMI Precipitation Algorithm

ERIC A. SMITH

Department of Meteorology and Supercomputer Computations Research Institute, The Florida State University, Tallahassee, Florida

F. JOSEPH TURK

Marine Meteorology Division, Naval Research Laboratory, Monterey, California

MICHAEL R. FARRAR

Department of Meteorology and Supercomputer Computations Research Institute, The Florida State University, Tallahassee, Florida

ALBERTO MUGNAI

Instituto di Fisica dell'Atmosfera-CNR, Frascati, Italy

XUWU XIANG

Department of Meteorology and Supercomputer Computations Research Institute, The Florida State University, Tallahassee, Florida

(Manuscript received 9 January 1996, in final form 1 July 1996)

ABSTRACT

This study presents research in support of the design and implementation of a combined radar–radiometer algorithm to be used for precipitation retrieval during the Tropical Rainfall Measuring Mission (TRMM). The combined algorithm approach is expected to overcome various difficulties that arise with a radar-only approach, particularly related to estimates of path-integrated attenuation (PIA) along the TRMM radar beam. A technique is described for estimating PIA at the 13.8-GHz frequency of the TRMM precipitation radar (PR) from 10.7-GHz brightness temperature T_B measurements obtained from the TRMM microwave imager. Because the PR measures at an attenuating frequency, an independent estimate of PIA is used to constrain the solution to the radar equation, which incorporates effects of attenuation propagation along a radar beam. Through the use of variational or probabilistic techniques, the independent PIA calculations provide a means to adjust for errors that accumulate in estimates of range-dependent rain rates at progressively increasing range positions from radar reflectivity vectors. The accepted radar approach for obtaining PIA from ocean-viewing radar reflectivity measurements is called the surface reference technique, a scheme based on the difference in ocean surface cross sections between cloud-free and raining radar pixels. This technique has encountered problems, which are discussed and analyzed with the aid of coordinated aircraft radar (Airborne Rain Mapping Radar) and radiometer (Advanced Microwave Precipitation Radiometer) measurements obtained during the west Pacific Tropical Ocean Global Atmosphere Coupled Ocean–Atmosphere Response Experiment in 1993. The derived relationship expressing 13.8-GHz PIAs as a function of 10.7-GHz T_B's is based on statistical fitting of many thousands of radiative transfer (RTE) calculations in which the relevant physical and radiative parameters affecting transmission, absorption, and scattering in a raining column and the associated emission-scattering properties of the wind-roughened ocean surface are systematically varied over realistic range intervals. The results demonstrate that the T_B–PIA relationship is stable, with a dynamic range up to about 8 dB. The RTE calculations are used to examine the relative merits of different viewing configurations of the radar and radiometer, and the associated uncertainty variance as the viewing configuration changes, since PIA uncertainty is an important control factor in the prototype TRMM combined algorithm.

1. Introduction

One of the scientific attractions of the Tropical Rainfall Measuring Mission (TRMM) is the possibility for development of combined instrument precipitation re-

Corresponding author address: Dr. Eric A. Smith, Dept. of Meteorology, Supercomputer Computations Research Institute, The Florida State University, Tallahassee, FL 32306-3034.
E-mail: esmith@metsat.met.fsu.edu

TABLE 1. Instrument system parameters of PR, TMI, and SSM/I.

Instrument	Operation	Frequency (GHz)	Resolution (km)	Polarization states
PR	35° inclination	13.8	4 (nadir)	Linear
TRMM	350-km altitude			
Precipitation	220-km swath			
Radar	±17° cross-track scan			
TMI	35° inclination	10.7	40	*V, H*
TRMM	350-km altitude	19.35	19	*V, H*
Microwave	758.5-km swath	21.3	18	*V*
Imager	49° conical scan	37.1	10	*V, H*
		85.5	5	*V, H*
SSM/I	98.8° inclination	19.35	56	*V, H*
Special Sensor	833-km altitude	22.235	50	*V*
Microwave	1394-km swath	37.1	32	*V, H*
Imager	45° conical scan	85.5	14	*V, H*

trieval algorithms. Because the TRMM satellite will carry both a multichannel microwave radiometer and a single-frequency incoherent precipitation radar, there is a particular focus on developing new algorithms that will exploit the respective strengths of these two rain-sensitive measuring systems [see Simpson et al. (1988), Simpson et al. (1996) and Theon et al. (1992) for a description of the TRMM instrument package]. Such algorithms, based on joint utilization of upwelling passive microwave brightness temperatures and range-gated radar reflectivities, are expected to improve upon single-instrument algorithms since the strengths of each instrument's measurements compensate, to some degree, for the weaknesses of the other (Hogg 1989).

The combined algorithm team of TRMM recently developed specifications for a first-generation radar–radiometer retrieval algorithm based on using path-integrated attenuation (PIA) information derived from the TRMM microwave imager (TMI), in conjunction with reflectivity measurements from the TRMM precipitation radar (PR) (see Smith 1995). Attenuation-corrected reflectivity algorithms, formulated in terms of raindrop size distribution (DSD) parameters, are an accepted approach for rain retrieval, assuming that the PIA is known a priori (see Meneghini and Nakamura 1990; Kozu and Nakamura 1991; Kozu et al. 1991). Because the TRMM PR measures at an attenuating frequency, it is critical that the raw reflectivities be adjusted for path attenuation (see Hitschfeld and Bordan 1954; Meneghini and Nakamura 1990; Marzoug and Amayenc 1991; Iguchi and Meneghini 1994). This study addresses the radiometer component of the prototype TRMM combined algorithm (or day 1 algorithm in the parlance of TRMM), which will be used to obtain PIA estimates at the PR frequency of 13.8 GHz. In essence, for combined retrieval, a technique is needed to obtain 13.8-GHz PIAs independent of PR measurements. This can be done using low-frequency brightness temperature T_B measurements from the TMI, a nine-channel, forward-viewing, conical-scanning passive microwave radiometer that will measure vertically/horizontally polarized T_B's at 10.65, 19.35, 37.0, and 85.5 GHz, along with vertical-only T_B's at 21.3 GHz. A description of the TMI is given in Simpson et al. (1996), while descriptions of the PR and the motivation for its design can be found in the articles of Awaka et al. (1988), Okamoto et al. (1988, 1991), Meneghini and Kozu (1990), and Nakamura et al. (1990). Table 1, which provides instrument characteristics of the TMI and PR, indicates that the two instruments have no common frequencies. However, because low-frequency brightness temperatures are well correlated with total path attenuation (Durden et al. 1995) and because there is good correlation between 13.8-GHz total path attenuation and this same quantity at nearby frequencies (Turk et al. 1995a–c), we investigate through radiative transfer (RTE) modeling how well the lower TMI frequencies, particularly 10.7 GHz, can be used to represent 13.8-GHz PIA.

Any PR-based retrieval scheme requires some type of correction for atmospheric-induced attenuation of the reflectivity signals (see Yeh et al. 1995). We first investigate why attenuation might best be obtained from radiometer measurements, rather than from the downward-looking, single-frequency, radar-based procedure called the surface reference technique (SRT). The SRT technique involves the difference between the measured ocean surface cross section of a rain column (σ_r^0) and the cross section of the rain-free ocean surface (σ^0) (see Meneghini et al. 1983; Meneghini et al. 1987; Meneghini et al. 1989; Fujita et al. 1985a; Fujita et al. 1985b). Since these quantities are derived from the radar measurements themselves, the use of the SRT technique in conjunction with a radar reflectivity algorithm does not constitute a combined algorithm in the sense defined above. However, that in itself is not a substantive criticism of a radar-only algorithm. The problem is that the SRT technique is prone to noise, partly due to variable wind and rain effects on surface roughness and partly due to the questionable underlying assumption that the surface roughnesses of rain-free and raining columns

are equivalent (see Meneghini et al. 1992). Thus, we evaluate a PIA parameterization scheme, relating 10.7-GHz brightness temperatures based on RTE modeling of simulated cloud–rain environments to 13.8-GHz path attenuation quantities calculated with the same model.

Combined radiometer–radar retrieval of precipitation represents a generally obscure, but not overlooked, topic in atmospheric remote sensing, dating back almost two decades. By the end of the 1970s, Lu and Hai (1980) had reported on the development of an X-band ground radar–radiometer system in China, for which they provided theoretical evidence that by making independent estimates of path attenuation, the resultant radar rainfall retrievals would improve over individual instrument methods. Later, Hai et al. (1985) went on to demonstrate such improvement with a dual-wavelength X–Ka-band system (9.375 and 35 GHz). They used an iterative retrieval scheme in which the radar path attenuations were constrained by radiometer brightness temperature estimates of the same quantities. A key result of that study was that by virtue of using an independent estimate of path attenuation, it was not necessary to obtain an absolute calibration of the radar constant, a problem that has plagued single-wavelength radar-based rain retrieval (see Iguchi and Meneghini 1994). Of course, their measuring scheme was limited by the elevated beam perspective of a surface platform (see Andrieu and Creutin 1995), and although this system did not mature to an operational rain retrieval system within China, in principle the approach heralded the down-looking method first tested on aircraft in the mid 1980s and now being developed for the TRMM mission using the PR and TMI instruments.

The first down-looking experiment involving rainfall retrieval from a simultaneous set of radar–radiometer measurements was reported by Fujita et al. (1985b). This involved an aircraft-mounted scatterometer/radiometer developed at the Communications Research Laboratory (CRL) in Japan (see Okamoto et al. 1982). However, the retrievals were made independently, not with a combined scheme. Weinman et al. (1990) were the first to test a truly combined scheme, again using measurements from the CRL airborne instrument package. In this study, a radiometer-derived PIA at the X band was used to help solve the Hitschfeld and Borden (1954) form of the radar equation at the X and Ka bands. The later studies of Kumagai et al. (1993a), Kumagai et al. (1993b), Meneghini et al. (1994), Schols and Weinman (1994), and Weinman et al. (1994) have continued to examine the aircraft-based combined algorithm approach. Alternatively, Vivekanandan et al. (1993), Turk et al. (1994), and Marzano et al. (1994) have addressed this problem using measurements from the airborne-mounted National Aeronautics and Space Administration (NASA) Advanced Microwave Precipitation Radiometer (Spencer et al. 1994) and the National Center for Atmospheric Research CP-2 pulsed Doppler radar (Vivekanandan 1990), though using separate retrieval schemes.

The aforementioned studies have viewed retrieval more from the perspective that the radar measurement is the strong element in the retrieval, while the radiometer measurement plays a supporting role—that is, the same philosophy behind the day 1 TRMM combined algorithm. Another class of algorithms is currently under study in which both radar and radiometer measurements play equivalent roles in an inversion process involving a coupled vector of radar reflectivities at multiple range gates and radiometer brightness temperatures at multiple windows. This approach, referred to as a ''tall vector'' scheme, proceeds on the basis that both radar and radiometers probe different depths in the rain columns, such that a unified radar–radiometer RTE model can achieve matchup to the extended measurement vector by manipulation of initial-guess or a priori rain profiles (see Smith et al. 1995b; Olson and Kummerow 1995; Marzano et al. 1995; Haddad et al. 1996b; Xiang et al. 1996; Farrar et al. 1996).

In the following, we explain the motivation behind the approach (section 2) and explain the radiative transfer modeling methodology used to relate PIA at one frequency to that at a nearby frequency (section 3). Section 4 goes on to describe the modeling results, while section 5 describes the functional relationship used to obtain PIAs at 13.8 GHz from 10.7-GHz T_B's. Section 6 provides a discussion of how higher-spatial-resolution radar measurements can be used to further refine rainfall estimates when used in conjunction with lower-resolution, diffraction-limited radiometer measurements. Section 7 explains the significance of the study and gives conclusions.

2. Motivation for the radiometer-based PIA approach

A radiometrically based path attenuation retrieval technique requires identical physical assumptions to be used for emission-based passive microwave rain-rate R retrieval. At the appropriate lower emission-driven frequencies, for a given ocean ''background state'' (defined by the underlying temperature–water vapor profile and surface temperature–emissivity boundary conditions), an increase in upwelling T_B is related mostly to increased liquid water content (LWC), and hence to R, within the atmospheric column, with the presence of suspended or precipitating ice hydrometeors having minor influence (see Jameson 1991; Smith et al. 1992; Mugnai et al. 1993). However, depending upon the characterization of the hydrometeor microphysics, T_B–R relationships using the standard 19-GHz emission frequency typically saturate beyond about 15 mm h^{-1} (Wilheit et al. 1977; Smith and Mugnai 1988). At 37 GHz, which is the highest microwave window frequency that provides meaningful emission signatures, saturation occurs below 5 mm h^{-1} (Savage and Weinman 1975; Smith and Mug-

nai 1988), and this frequency is sensitive to ice particles. For the 19–37-GHz frequency range, there is a significant response to nonprecipitating cloud liquid water as well (Smith and Mugnai 1988; Lhermite 1988), so that cloud droplets, particularly the larger ones, tend to bias rain-rate estimates high. Alternatively, because characteristic ground footprint sizes of current passive microwave instruments such as the Special Sensor Microwave/Imager (SSM/I; see CalVal 1989) are greater than the 1–2-km dimensions of typical precipitation cells (Table 1 includes a summary of SSM/I instrument parameters), incomplete beam filling biases rain-rate estimates low because of the underlying concave upward curvature of the characteristic nonlinear T_B–R relationships intrinsic to emission frequencies.

Use of a lower frequency, such as 10.7 GHz, mitigates the problems with nonprecipitating cloud water and ice particles, while effectively extending the dynamic range of the T_B–R relationship to higher rain rates. In practice, the full benefits of this dynamic range improvement are not immediately realized because characteristic 10.7-GHz beam sizes are overly large due to the diffraction-limited nature of radiometer measurements (see Janssen 1993). For example, the 10.7-GHz footprint size of the *Nimbus-7* Scanning Multichannel Microwave Radiometer instrument is about 100 km. Even with the low orbit of TRMM (350 km), the 10.7-GHz footprint size of TMI is approximately 40 km. By the same token, spatial deconvolution techniques such as those described by Farrar and Smith (1992), Robinson et al. (1992), and Farrar et al. (1994) can be used to achieve some resolution gain since there will be significant overlap in the TMI 10.7-GHz beams. Notably, the smaller atmospheric optical depths at 10.7 GHz will place greater emphasis upon a correct characterization of surface radiometric properties. Furthermore, the no-rain T_B threshold, which depends largely upon surface characteristics and the water vapor profile, is important for establishing an adequate no-rain attenuation reference level. Therefore, in this study, we place special emphasis upon modeling the wind-roughened ocean surface to examine T_B response to variations in sea surface temperature and surface wind speed (U). In doing so, we use a surface emissivity model that is a function of frequency, view angle, salinity, and U.

The radar-based, single-frequency SRT, which is used in radar rain retrieval at the higher attenuating frequencies, is based on the difference between a climatologically defined rain-free ocean surface cross section (σ^0) and the observed surface cross section in the presence of rain (σ_r^0) (see Meneghini et al. 1983; Meneghini et al. 1987). The rain-free σ^0 establishes a reference value for which the one-way total path attenuation A can be obtained by the relation $A = (\sigma^0 - \sigma_r^0)/2$, where the factor of 2 accounts for a two-way path. Tests of the SRT using aircraft measurements, and its extension to dual radar frequencies (the DSRT technique), have been discussed and studied by Meneghini et al. (1987); Meneghini et al. (1989), and Iguchi and Meneghini (1994). One of the pressing issues as the TRMM launch approaches is whether the uncertainties associated with such attenuation estimates will require assuming idealized rain-rate distribution functions over extended time–space scales to inhibit noise generation in the retrievals at instantaneous pixel scales (see Meneghini and Jones 1993). Such an assumption is already in use for the monthly 5° surface rain-rate algorithm being developed for the TMI (see Wilheit et al. 1991).

TABLE 2. AMPR radiometer system parameters (Spencer et al. 1994). Based on an ER-2 aircraft altitude of 20 km and an airspeed of 500 mph. Polarization state skews are received from pure horizontal at scan start, to linear 45° at nadir, to pure vertical at scan end.

Frequency (GHz)	Swath width (km)	Beam width (°)	Nadir FOV (km)	Polarization
10.7	40	8.0	2.8	*H* to *V* skew
19.35	40	8.0	2.8	*H* to *V* skew
37.1	40	4.2	1.5	*H* to *V* skew
85.5	40	1.8	0.6	*H* to *V* skew

a. Use of AMPR–ARMAR measurements from TOGA COARE

For this study we analyze aircraft radiometer and radar data to help shed light on how well the SRT technique performs under actual conditions. The NASA Marshall Space Flight Center Advanced Microwave Precipitation Radiometer (AMPR) includes channels at 10.7, 19, 37, and 85 GHz [see Spencer et al. (1994) for an instrument description]. This package, which can be used to some degree as a high-resolution airborne simulator of the TRMM TMI, was flown in early 1993 onboard the NASA ER-2 high-flying aircraft during the Tropical Ocean Global Atmosphere Coupled Ocean–Atmosphere Response Experiment (TOGA COARE) over the tropical western Pacific warm pool [see Webster and Lukas (1992) for a description of TOGA COARE]. Table 2 provides a summary of AMPR instrument parameters. The AMPR scans ±45° across track, acquiring 50 pixels per scan. Each scan requires 3 s, during which the ER-2 moves forward about 600 m at its nominal airspeed of 200 m s^{-1}. AMPR calibration is accomplished by viewing upward to stare at hot–cold loads after every fourth scan. In 1992, the calibration loads were replaced with an improved return-loss material, which also exhibits smaller thermal temperature gradients across the region where the feedhorn views. Unlike the conical-scanning SSM/I and TMI, the AMPR's receive polarization state does not remain constant across the scan, skewing from *H* to *V* (right to left as viewed by the pilot), passing through a 45° linear state at nadir. Therefore, it is not possible to extract true scene *H* and *V* T_B's except at the scan end points. For clear skies over oceans, the skew is detectable as a gradual

TABLE 3. ARMAR radar system parameters (Durden et al. 1994).

Frequency	13.8 GHz
Scan limits	±20 °
Swath width	9 km
Nadir resolution	800 m
Range resolution	80 m
Polarization states	*HH, VV, HV, VH*
Aperture diameter	0.4 m
Antenna gain	34 dB
3-dB beamwidth	3.8°
Sidelobe level	−32 dB
Polarization isolation	−28 dB
Peak power	200 W
PRF	1–8 kHz
Pulse duration	5–45 μs
Chirp bandwidth	4 MHz

T_B warming across each scan, due to the higher vertically polarized emissivity of the ocean surface. However, over the range of ±15°, the polarization state is relatively constant at 45° linear. Since net upwelling radiation is largely unpolarized near nadir, it is possible to use the AMPR measurements quantitatively within the ±15° swath, where the assumption that the scene $T_B^V \approx T_B^H$ is warranted (see Vivekanandan et al. 1993; Smith et al. 1994c).

During TOGA COARE, AMPR data acquisition was occasionally coordinated with the scanning of the NASA Jet Propulsion Laboratory (JPL) 13.8-GHz Airborne Rain Mapping Radar (ARMAR) onboard the NASA DC-8 aircraft, whose 10-km flight altitude is about half that of the ER-2 and that nominally flies slightly faster. The ARMAR is the aircraft prototype of the TRMM PR, although it is a more versatile instrument and includes as part of the instrument package, a 13.8-GHz scanning radiometer channel [see Durden et al. (1994) for a description of ARMAR]. Table 3 provides a summary of ARMAR instrument parameters. Unlike the PR, which is power limited, the ARMAR is coherent and employs pulse compression to achieve low-range sidelobe levels, which can otherwise mask rain signals near the ocean due to the presence of a strong return from the ocean's surface (Tanner et al. 1994). Twelve straight line storm overpasses with well-coordinated ER-2 and DC-8 flight lines have been identified in the TOGA COARE aircraft logs on 4, 8, 20, and 22 February 1993 (see Yuter et al. 1995). The individual AMPR and ARMAR scans were initially aligned using the inertial navigation-based latitude–longitude coordinates from the two aircraft and then fine-tuned by empirical adjustment so that the nadir traces of the AMPR 10.7–19-GHz T_B's were optimally correlated with the nadir traces of the ARMAR 13.8-GHz T_B's. The best coordinated flight lines occurred on 4 and 8 February.

Two such flight lines are presented in Figs. 1a,b. The scan scenes in Fig. 1a are from 4 February 1993 over convection lines near the developing eye of an incipient tropical cyclone (Oliver) that spawned south of the TOGA COARE study area. The scenes in Fig. 1b are from 8 February (4 days later), after the cyclone intensified and when the flight lines of the ER-2 and DC-8 crossed over a sequence of spiral outer bands before penetrating a well-established cyclone eyewall. The two figures illustrate ARMAR reflectivities at 500 m above the surface (leftmost panels) and AMPR upwelling brightness temperatures at all four AMPR frequencies (four rightmost panels). The 4 February images indicate two broad convection bands centered near scans 55 and 140, identifiable by elevated radar reflectivities, T_B warming at 10.7–19 GHz, and selective scattering at 37–85 GHz. The first band shows peak reflectivities of approximately 40 dB*Z* but little evidence of high-frequency scattering, suggesting warm rain convection and/or stratiform rain with only small ice particles. The second band is actually divided into two separate lines. The first, between scans 120 and 140, contains a significant amount of large ice particles and heavy rain evident from the strong scattering-induced T_B depressions at 37 and 85 GHz (e.g., T_B-85's < 100 K), nearly saturated T_B's at 10.7 GHz (~280 K), and peak radar reflectivities of about 45 dB*Z* at scan 140. Notably, the radar reflectivity profiles around scan 120 exhibit artifacts of strong propagation attenuation. The second line around scan 160 is narrower and weaker, but contains enough large ice particles to produce a distinct 85-GHz scattering signature (T_B-85's between 125 and 150 K) and radar reflectivities just shy of 40 dB*Z*. The main features in Fig. 1b are the elevated ARMAR reflectivities and AMPR 10.7–19-GHz T_B's produced by three outer convection bands centered near scans 25, 75, and 125, plus these same elevated reflectivity warming signatures at the cyclone eyewalls as the two aircraft penetrated and exited the storm center (scans 200 and 250, respectively). Note that the ARMAR flight segment is missing during the exit period. The cyclone eye, centered near scan 225, is readily apparent in all of the ARMAR and AMPR panels.

b. Shortcomings of SRT-based PIA estimates

The nadir traces of these two flights are analyzed and presented in Figs. 2a,b to illustrate the problem with the SRT scheme and to explain the motivation behind the radiometer-based attenuation approach. Each of these figures consists of four panels. The upper-left panels contain the AMPR 10.7- and 19-GHz T_B's, along with 13.8-GHz T_B's from ARMAR. For both flights, with few exceptions, the magnitudes of the T_B's increase with increasing frequency (i.e., optical depth monotonically increases with frequency), suggesting that extinction is virtually controlled by liquid water processes. Upper-right panels contain the 500-m level (Z_{500}) and surface level (Z_s) ARMAR reflectivities. Note that the JPL format converts all range gates to dB*Z* (mm^6 m^{-3}); therefore, gates that intersect the ocean surface are not expressed in terms of the usual definition of surface cross

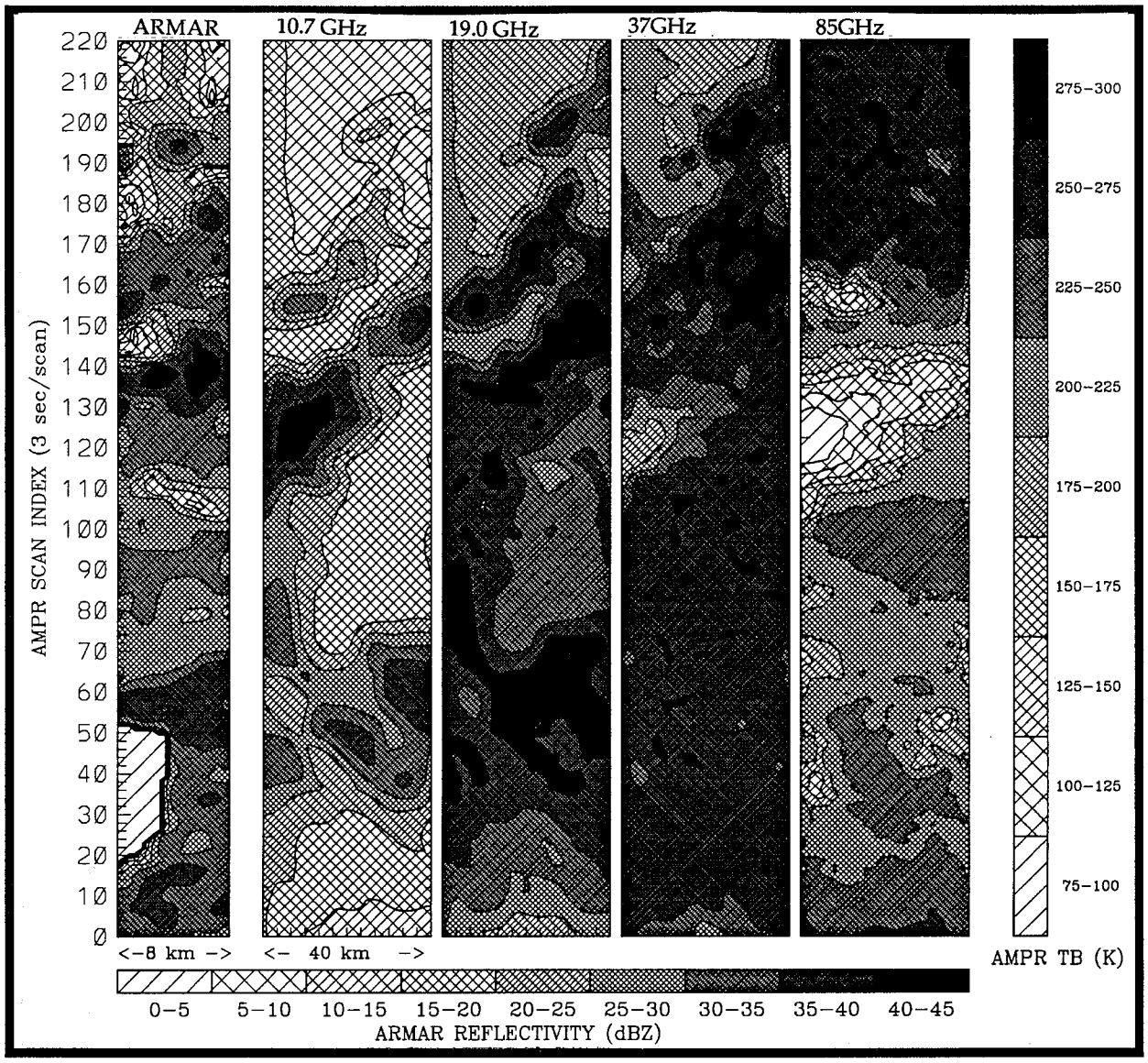

FIG. 1a. Coordinated ER-2/DC-8 flight data from 4 February 1993 TOGA COARE mission, representing an approximately 150-km flight track or 220 AMPR scans. Four rightmost panels show AMPR scan imagery of upwelling T_B's across a 40-km swath over an 11-min time period (1901:30–1912:31 UTC), with T_B scale on right. Leftmost panel shows ARMAR scan image of constant altitude PPI (CAPPI) reflectivities at 500 m above surface (Z_{500}) across an 8-km swath over a 10.16-min time period (1858:30–1908:39 UTC), with Z scale on bottom. The flight progresses from smaller to larger scan numbers (bottom to top of panels) representing a ground track from north to south (13.16°S, 147.07°W to 14.18°S, 147.68°W) Note the ER-2 and DC-8 aircraft are not exactly time synchronized; the DC-8 enters the segment 3 min prior to the ER-2 and travels at a higher airspeed completing the segment about 50 s quicker than the ER-2. The nadir scan position is down the center of the image panels. The cross-track distance scale of the ARMAR panel is magnified for display purposes. Missing data in the ARMAR panel are indicated with blanks.

section σ^0. The appropriate conversion at nadir is $\sigma^0 \approx Z_s - 71.3$ (S. Durden 1995, personal communication). It is evident that clear-sky (unattenuated) Z_s values are around 81 dBZ (i.e., σ^0's of about 10 dB). The Z_{500} peaks for both flights show evidence of propagation attenuation. A reflectivity profile from a single ARMAR beam through stratiform rain is shown in Fig. 3 to help interpret the Fig. 2 reflectivity panels. A bright band near 4.6 km is evident, while the 0-dBZ cloud top is found just above 8 km. The peak reflectivity below the bright band is 35 dBZ, corresponding to a rain rate of 4 mm h^{-1} (see Fig. 4). The ocean Z_s is ~78 dBZ (indicated by the spike at 0 km), and based on an 81-dBZ clear-sky value, this suggests a one-way path attenuation of about 1.5 dB. From Fig. 4, at 13.8 GHz, characteristic attenuation rates are 1.5 dB km^{-1} for a rain rate of 35 mm h^{-1}. Here, attenuation κ (dB km^{-1}) is calculated from the Nakamura et al. (1990) expression $\kappa =$

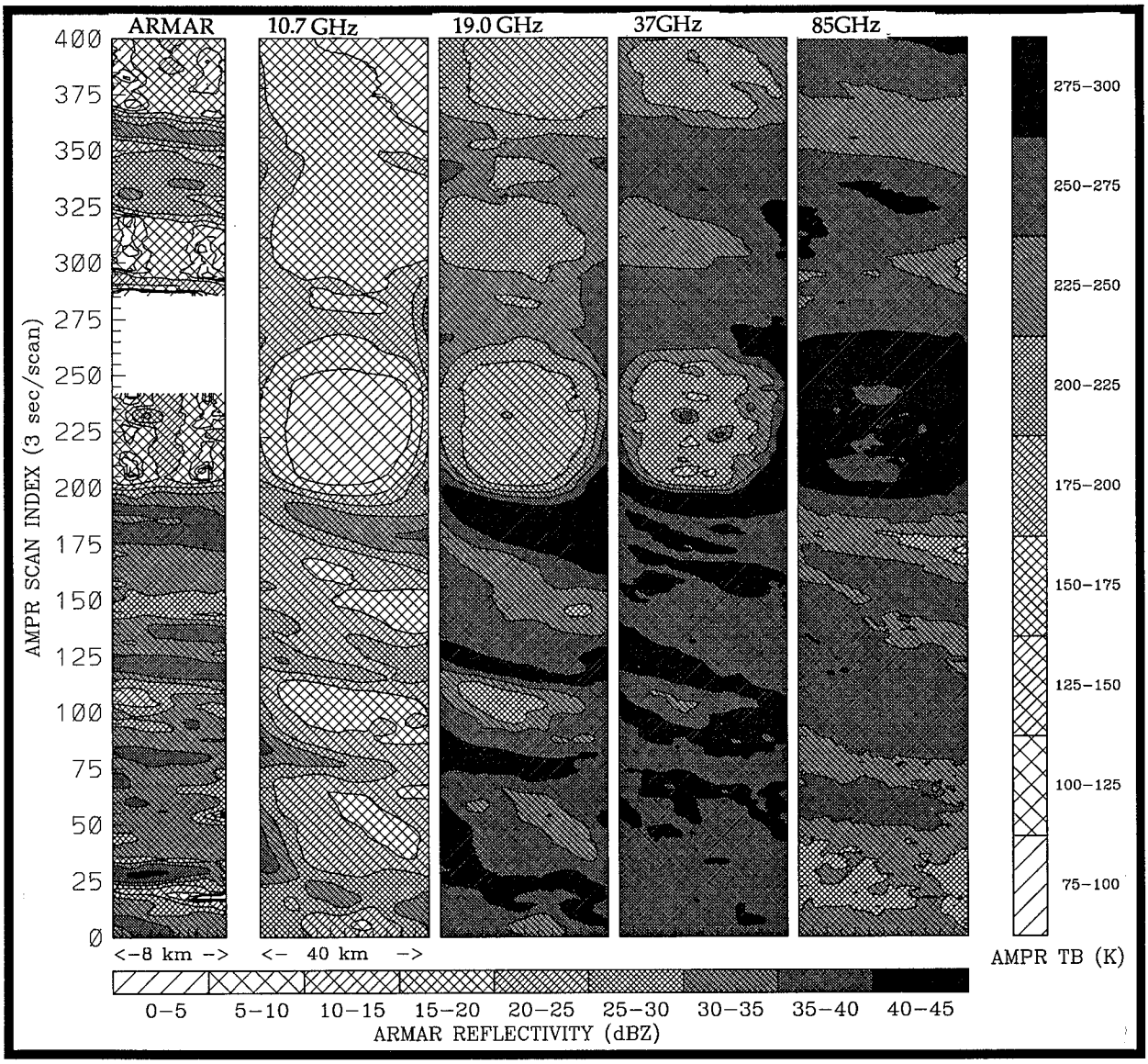

FIG. 1b. Same as Fig. 1a except for 8 February, representing a 275-km flight track or 400 AMPR scans. AMPR scan imagery is over a 20-min time period (2045:00–2105:00 UTC), while ARMAR scan imagery is over a 19.67-min time period (2044:30–2104:10 UTC). The flight progresses from southeast to northwest (19.30°S, 150.99°W to 18.42°S, 153.09°W). As with the 4 February flight, the ER-2 and DC-8 flight lines are not exactly time synchronized. As before, missing data in the ARMAR panel are indicated with blanks.

$0.032R^{1.124}$, based on Olsen et al. (1978) (see also Haddad et al. 1995; Haddad et al. 1996a).

The lower-left panels in Figs. 2a,b show one-way path attenuations calculated from both the SRT method and the 10.7-GHz radiometer method under study here, while the lower-right panels show the associated rain rates based on an attenuation-corrected Z–R relationship. The SRT-based attenuation A(SRT) (dB) is given by $(81 - Z_s)/2$ (as discussed above), in which 81 dBZ is taken as the clear-sky surface reflectivity, whereas the T_B-based attenuation $A(T_B)$ is given by $21.8605 - 4.286 \ln(285.87 - T_B)$. The formulation of the $A(T_B)$ expression and its associated coefficients will be discussed in detail in section 5. For the present, it is only important to note that there are significant differences between the A(SRT) values and the $A(T_B)$ values. In Fig. 2b, the A(SRT) values run consistently higher, suggesting a simple bias between the two techniques. However, the 4 February results (Fig. 2a) indicate larger A(SRT)'s for the first convection band, followed by smaller values for both the heavy and light rain events in the second band. This clearly precludes the systematic bias explanation.

The Z–R relationship used to produce the rain rates in the lower-right panels is given by $\tilde{Z} = 372.4R^{1.54}$, where $\tilde{Z}$ is adjusted for propagation attenuation accord-

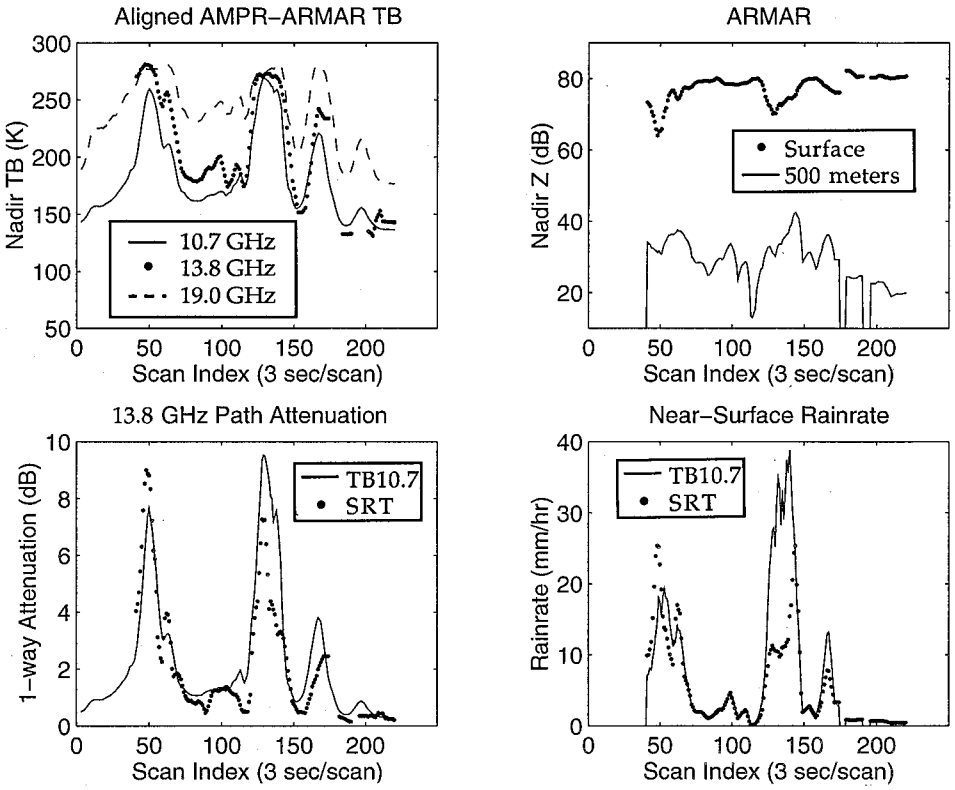

FIG. 2a. Nadir flight track data from coordinated 4 February 1993 ER-2/DC-8 mission (AMPR times of 1901:01–1912:00 UTC). The four panels contain (clockwise from upper left) (i) AMPR 10.7- and 19-GHz T_B's, along with ARMAR 13.8-GHz T_B's; (ii) ARMAR reflectivities at 500-m level and at range gate intersecting ocean surface; (iii) rain rates at 500-m level based on *Z–R* calculations using both SRT-based attenuation correction and 10.7-GHz radiometer-based attenuation correction; and (iv) one-way 13.8-GHz path attenuations derived from SRT and 10.7-GHz T_B techniques.

ing to $\tilde{Z} = Z + 1.8A$, with the attenuation A taken as either A(SRT) or $A(T_B)$. The 1.8 factor is obtained by 2×0.9, where 2 accounts for two-way path attenuation and 0.9 comes from assuming that the attenuation correction is applied to a Z_{500} measurement obtained within a 5-km rain layer exhibiting uniform attenuation along the vertical path. The coefficients of the *Z–R* relationship are given in Nakamura et al. (1990) (see also Ulbrich 1983). In such calculations, a rain-rate difference is consistent with an attenuation difference (if an SRT-based PIA is smaller/larger than a T_B-based PIA, then an SRT-corrected rain rate is smaller/larger than a T_B-corrected rain rate) and increases as the baseline reflectivity increases, in accordance with the nonlinear properties of the *Z–R* power law. It is evident that the differences between the A(SRT) and $A(T_B)$ quantities make little difference to the retrieved rain rates for the lower dB*Z* range (say, below 35 dB*Z*), but above that threshold they give rise to significant rain-rate differences (see Fig. 4). From Figs. 2a,b, differences range from around 5 mm h^{-1} for various events on 4 February (scans 50 and 165) and 8 February (scans 15, 120, 135, and 190) over 20 mm h^{-1} for the heavy rainband on 4 February (scans 120–125). Although part of the differences can be attributed to noncongruous fields of view, these effects do not outweigh the inherrent differences in the SRT- and T_B-based PIA estimation schemes.

The underlying assumption of the SRT is that the surface roughness remains constant when observing either rain-free or raining regions, meaning that the σ_r^0 of the raining column with the rain removed would be equivalent to the σ^0 of the rain-free column. However, differing surface winds create different roughness properties within and outside of precipitation cells, and within the precipitating regions the rain itself will impact the capillary wave structure. Thus, this assumption is expected to lead to problems. For example, Fig. 5a shows that ARMAR radar measurements from a 22 February 1993 DC-8 flight over both warm and cold rain clouds exhibit variations in rain-free σ^0's as high as ±5 dB near nadir where the specular radar return is largest (local mean is about 81 dB*Z*). The radar reflectivities are plotted as a function of 13.8-GHz ARMAR-measured radiometer brightness temperatures. This result is indicative of the level of noise inherent to the SRT method. A more thorough examination of the noise contained just within the clear-sky σ^0's is given in Fig. 5b, in which a carefully selected set of rain-free scenes

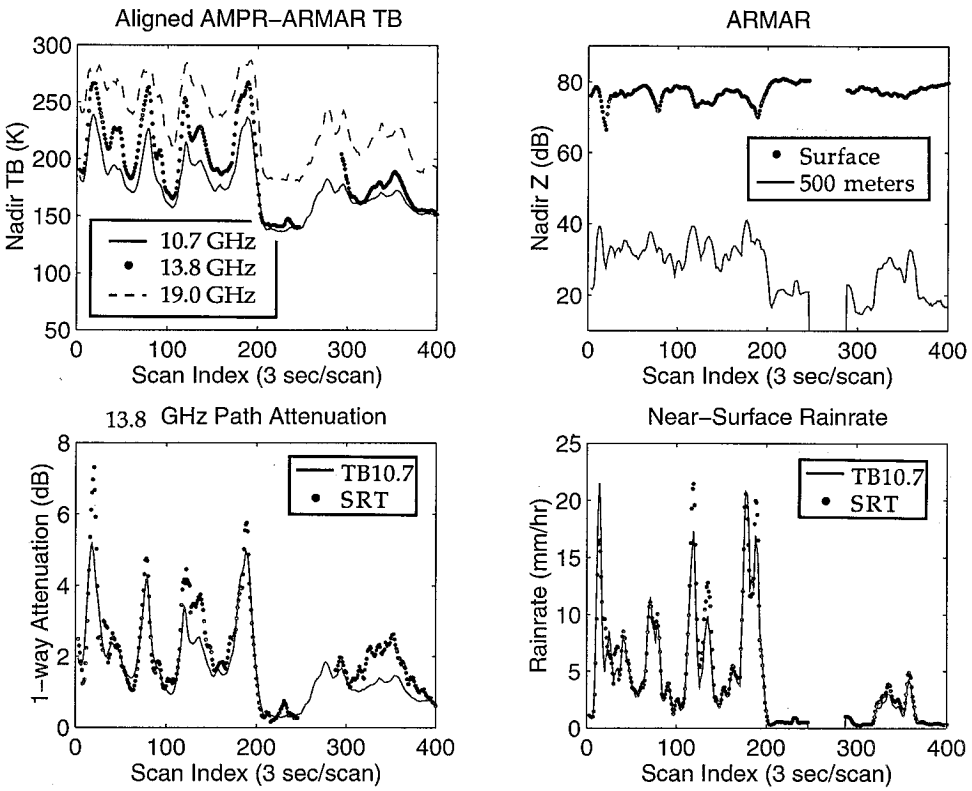

FIG. 2b. Same as Fig. 2a except for 8 February (AMPR times of 2044:03–2104:12 UTC).

(1157 pixels) from the 12 coordinated TOGA COARE flights are considered. A 10.7-GHz T_B threshold of 150 K is used to isolate rain-free columns. This is equivalent to a T_B-derived attenuation of ~0.8 dB of which some 0.15 is due to water vapor and the remaining 0.65 is due to nonprecipitating cloud. The corresponding radar Z_s's and $A(T_B)$'s are plotted in both scatter diagram form and as individual histograms. The mean Z_s is 81.8 dBZ (with a mode of 81 dBZ), while the mean $A(T_B)$ is 0.49 dB. It is clear that the spread of Z_s (~±3 dB) exceeds that of $A(T_B)$ (~±0.3) by an order of magnitude, demonstrating why it is worth considering a radiometer-based correction for propagation attenuation.

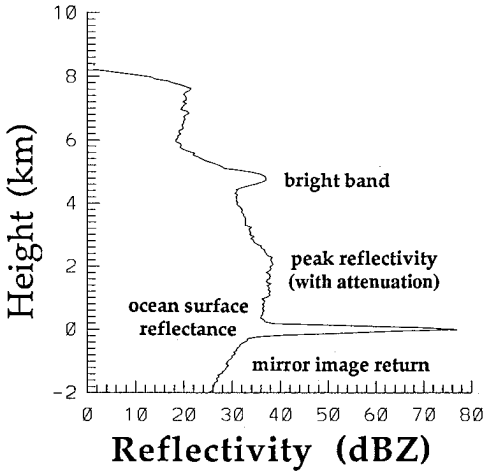

FIG. 3. ARMAR reflectivity profile from a single ARMAR nadir beam (time is 2136:15 UTC 8 February 1993 and position is 19.64°S, 152.15°W). Positions of bright band, peak reflectivity, surface return, and mirror image return are indicated.

In practice, a value of σ^0 is best obtained by locating a rain-free region nearest the rain region both spatially and temporally, and using the average $\langle\sigma^0\rangle$ in that region as a reference. This reduces noise in the rain-free term. The problem comes from the rain column term since each σ_r^o realization involves wind and rain effects on the surface, distinct from effects associated with $\langle\sigma^0\rangle$. Moreover, recent analysis of observations from the navy's 1978 Seasat synthetic aperture radar suggests that the impact of raindrops upon the ocean results in a ''smoothing'' of the surface (see Atlas 1994). If so, because of the increased specular properties of the smoother surface, one would expect a smaller surface return as the radar scans away from nadir. By the same token, Durden et al. (1995) have compared 13.8-GHz radar- and radiometer-derived path attenuations over oceans using ARMAR data, and for a range of path-averaged rain rates between 0 and 40 mm h^{-1}, found small systematic bias of the SRT (0.7 dB at nadir and 1.7 dB at 10° view angle). However, similar to what is

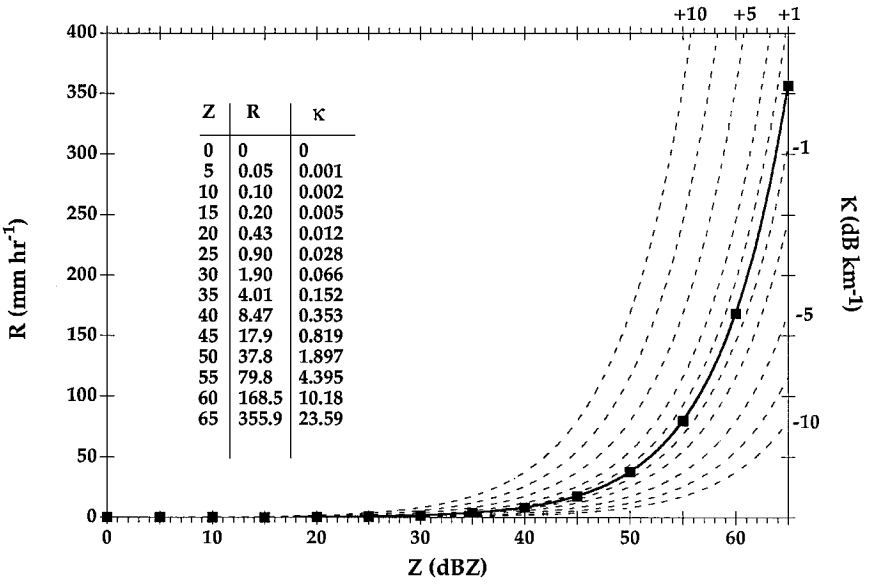

FIG. 4. Relationship between rain rate, attenuation, and effective reflectivity, along with rain-rate error curves for various fixed reflectivity errors. Thick solid line indicates a baseline relationship of $Z = 372.4R^{1.54}$, with Z in dBZ units (mm^6 m^{-3}) and R in millimeters per hour. The table provides attenuation κ (dB km^{-1} numerically, associated with a sequence of Z's and R's, using $\kappa = 0.032R^{1.124}$. In the table, the Z's are incremented by 5 dB from 0 to 65 dBZ, and those Z abscissas are indicated with solid squares on the baseline Z–R curve. Thin dashed lines indicate Z–R relationships assuming positive and negative reflectivity errors of 1, 2.5, 5, 7.5, and 10 dB. The Z–R and κ–R relationships are from Nakamura (1990).

seen in our Figs. 5a,b, the scatter inherent to the attenuation relationship given in their paper exceeds ±7 dB taken with respect to either axis; at reflectivities of, say, 50 dBZ, such errors translate to errors exceeding 100% in retrieving surface rain rate (see Fig. 4).

3. Modeling cloud–rain column

In order to make representative attenuation calculations with radiometer measurements, we incorporate an RTE model in conjunction with physical descriptions of both warm- and cold-rain-type precipitating clouds. ARMAR radar measurements obtained during TOGA COARE show that heavy rain often results from precipitating clouds containing highly variable amounts of ice above the melting level. In some situations, the top of the ice region (as defined by reflectivities in the 0–10-dBZ range) ranged up to only about 7 km and was usually associated with a narrow radar bright band indicative of stratiform rain, while more convective situations produced ice tops above the DC-8 altitude of approximately 11 km. The latter situation showed reflectivity enhancement spread above the normal 4.6-km melting level and evidence of strong rain attenuation in and below the enhanced region. In extreme cases, the attenuation was so severe that the vertical reflectivity profile gave the general appearance of a radar bright band, when, in fact, the decrease in radar reflectivity below the melting level was due to cumulative two-way path attenuation. Careful scrutiny of these cases indicates that the false brightband signatures do not exhibit the expected vertical attenuation structure of the bright-band region, with one type of attenuation slope above

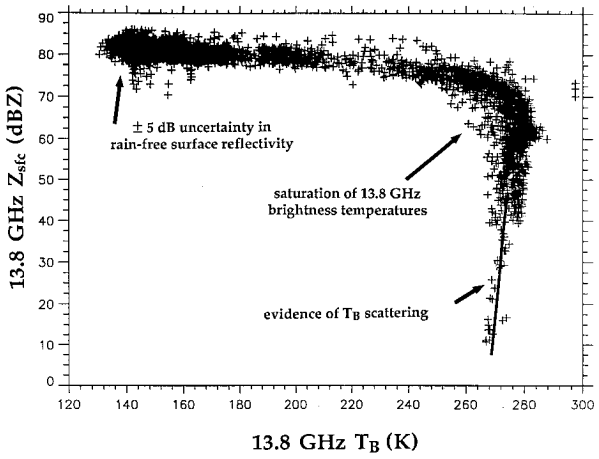

FIG. 5a. Variation of ARMAR-derived surface nadir reflectivity at 13.8 GHz as a function of 13.8-GHz T_B (all beams selected within 3° of nadir). Measurements were obtained on 22 February 1993 during a 2-h DC-8 flight south of the TOGA COARE study area. The reflectivities associated with the rain-free pixels (T_B's colder than 150 K) exhibit a variation of about ±5 dB around an 81-dBZ baseline, with outliers as low as 73 dBZ. The point at which T_B saturation occurs is indicated, as well as a region of positively sloped large T_B's, indicative of scattering.

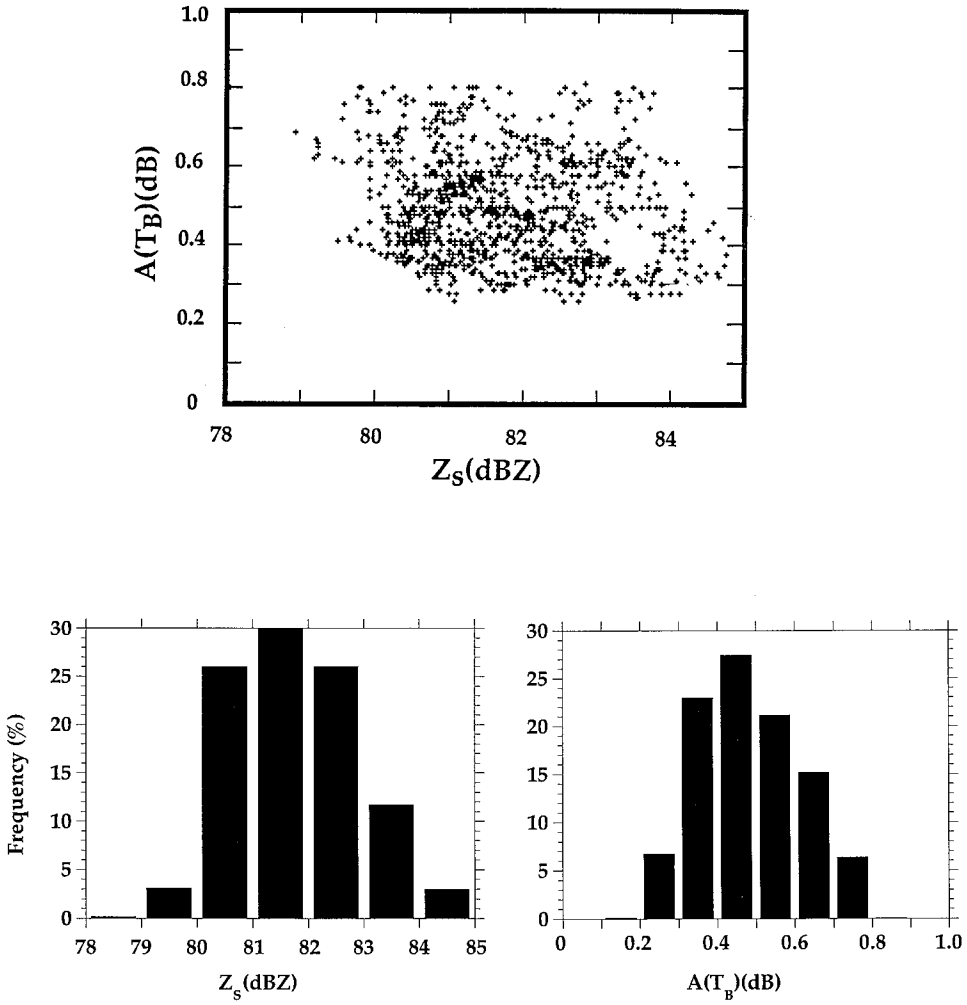

FIG. 5b. Scatter diagram (top panel) and individual histograms (bottom panels) of Z_s's and $A(T_B)$'s obtained for 1157 coincident ARMAR–AMPR rain-free scenes selected from the 12 coordinated DC-8/ER-2 TOGA COARE flights. The mean Z_s is 81.8 dBZ (modal value is 81 dBZ), with a spread of ±3 dB, while the mean $A(T_B)$ is 0.49 dB, with a spread of ±0.3 dB.

the reflectivity peak arising from aggregate melting and another below the peak arising from aggregate breakup.

Although attenuation from ice is weak at 13.8 GHz (to be addressed in the discussion of Fig. 8), ice scattering strongly affects radiometric measurements at and above 19 GHz. Hence, any attempt to relate 10.7- or 19-GHz T_B's to path attenuation will be different for the differing cloud structures. In order to understand the potential for radiometrically estimated 13.8-GHz rain attenuation, both types of clouds (as described above) have been simulated by specifying different levels of cloud-top height and vertical distributions of liquid water and ice mass contents associated with suspended and precipitating hydrometeors. For both types of structures, simulations are performed for a wide variety of microphysical conditions (size distributions and ice densities), SSTs, surface wind speeds, and temperature–water vapor profiles. However, the hydrometeor properties are taken as uniform along the vertical profile. The allowed variations applied to each relevant model parameter are described in Table 4.

Some 200 TOGA COARE radiosondes (TCIPO Staff 1993), taken over the January–February 1993 period near Kavieng (northeast of Papau, New Guinea, on the Bismarck Archipelago) were used to generate representative variability in vertical temperature–water vapor structure. Precipitable water amounts range from 4.0 to 6.5 cm.

For purposes of the attenuation analysis, 50 cloud simulations were performed for each of the soundings (producing a total of 10 000 RTE calculations), where each simulation consisted of a randomly generated cloud microphysical structure within the bounds given in Table 4. Here, microphysical structure pertains to cloud-, rain-, and ice-layer geometries, the LWC/ice water content of the liquid and frozen layers, and the ice density.

TABLE 4. Range of variation of cloud column, microphysical parameters, sea surface temperature, surface wind speed, and precipitable water used in RTE modeling.

Rain-layer base (km)	0
Rain-layer top (km)	4–5
Ice-layer top (km)	4–15
Cloud-layer base (km)	2
Cloud-layer top (km)	2–7
Rain LWC (g m^{-3})	0–3
Ice equivalent LWC (g m^{-3})	0–3
Cloud LWC (g m^{-3})	0–1
Ice density (g cm^{-3})	0.4–0.9
Median drop size D_o (mm)	0.8–2.5
Gamma shape parameter (m)	0–4
Sea surface temperature SST (K)	293–303
Surface wind speed U (m s^{-1})	0–30
Precipitable water PW (cm)	4.0–6.5

A gamma drop size distribution of the form $N(D) = N_0 D^m \exp(-\Lambda D)$ was adopted for the rain and ice hydrometeors (taken as spheres), where D is drop diameter, N_o is the peak concentration at median drop size D_o, and m and Λ are referred to as the shape and slope parameters. The median drop size D_o is given by $(3.67 + m)/\Lambda$. In the RTE calculations, D_o and m are specified (randomly), thereby fixing Λ and N_o. It remains to specify SST, U, and the radiometer view angle from nadir for the RTE calculations. The ocean surface model and microwave RTE model are described below.

Our assumption that hydrometeors can be adequately represented by equivalent volume spheres is based upon the model study of Turk and Vivekanandan (1995), who considered the effects of hydrometeor shapes upon ground- and space-based microwave T_B measurements. Using equilibrium-sized oblate spheroidal shapes for rain and conical-shaped graupel particles, RTE calculations were compared against equivalent-volume spherical shapes for a variety of rain rates and ice-layer optical thicknesses. At 10.7 GHz, the radiative effects of ice hydrometeors are small, and thus the upwelling T_B's are largely independent of hydrometeor shape. At 85 GHz, conical-shaped graupel particles were shown to be responsible for 15°C polarization difference, in accord with an analysis of SSM/I measurements reported by Spencer et al. (1989) [see also Evans and Vivekanandan (1990) for a study of the polarization induced by nonspherical ice particles at higher microwave frequencies]. As will be discussed, the attenuation model developed in this paper uses 10.7-GHz T_B as the independent variable, so that the assumption of spherical hydrometeors in the development of the T_B–attenuation relationship is warranted.

a. Ocean surface emissivity modeling

A commonly used assumption for ocean surface emissivity is that it exhibits the properties of a Fresnel surface, where the horizontal and vertical emissivity coefficients (ϵ_H and ϵ_V) are functions of view angle and the ocean water dielectric constant, the latter being a function of temperature, frequency, and salinity (Klein and Swift 1977). At the microwave frequencies considered here, the salinity dependence is weak, while warmer oceanic temperatures tend to reduce the emissivity, especially above 37 GHz. For example, the nadir 85-GHz Fresnel emissivity drops from 0.575 to 0.540 when the ocean temperature increases from 293 to 303 K. Petty and Katsaros (1994) have provided calculations showing the behavior of ϵ_H and ϵ_V coefficients at SSM/I frequencies.

In general, Fresnel coefficients are not realistic since wind disturbs the ocean surface enough that it does not exhibit mirror surface properties. Therefore, the Fresnel emissivities should be considered as lower bounds on the actual emissivities given the possibility of a roughened sea. A number of studies have parameterized the surface emissivity as a function of wind speed, with the different parameterizations exhibiting their greatest dispersion at higher wind speeds. Using a bivariate Gaussian distribution of ocean surface slopes derived from sun glint photographs, Wilheit (1979) took a geometric optics approach to account for the effect of wind speed roughening of the ocean surface. In this method, the Fresnel emissivities are averaged over the slope distribution for each polarization state. Using the same principles, Petty and Katsaros (1994) presented a mathematically rigorous formulation underlying the geometric optics approach and applied it to SSM/I frequencies at the appropriate view angle for obtaining wind-dependent changes in slope variance. The results were parameterized as deviations ($\Delta\epsilon$) from the Fresnel emissivities. For increases in the slope variance, they found an increase and decrease in the values of ϵ_H and ϵ_V compared to Fresnel values, thereby producing a net reduction in the upwelling T_B polarization difference for clear sky conditions. While producing significant changes in the emissivity values away from nadir, the Petty and Katsaros formulation does not significantly affect emissivity at nadir, as expected for the Gaussian form of slope variation.

In our analysis, we have added the contribution due to foam as described by Wilheit (1979), which is essentially a wind-dependent correction term that is added onto the wind-roughened emissivity values. As this correction term is radially independent, it acts to increase the emissivities at all view angles, including nadir. Plots of the overall ϵ_H and ϵ_V quantities at the window frequencies of TMI are shown in Fig. 6 for surface wind speeds of 0, 10, 20, and 30 m s^{-1}. For a more comprehensive review, we refer to the article by Petty and Katsaros (1994).

b. Radiative transfer modeling

Upwelling brightness temperatures and path-integrated attenuations have been calculated from nearly equivalent RTE models described by Smith et al.

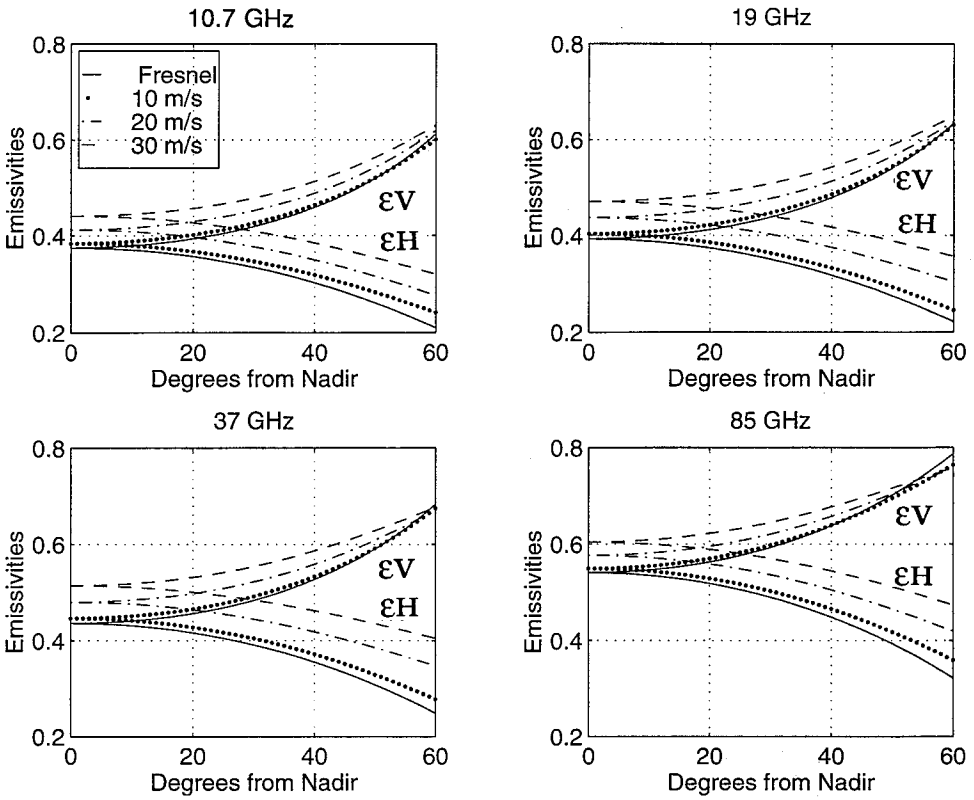

FIG. 6. Variations in Fresnel and wind-roughened sea surface emissivities (for both vertical and horizontal polarizations) at 10.7, 19, 37, and 85 GHz as function of view angle. Calculations are based on the model of Petty and Katsaros (1994) and a foam correction term given by Wilheit (1979). The SST is taken as 303 K.

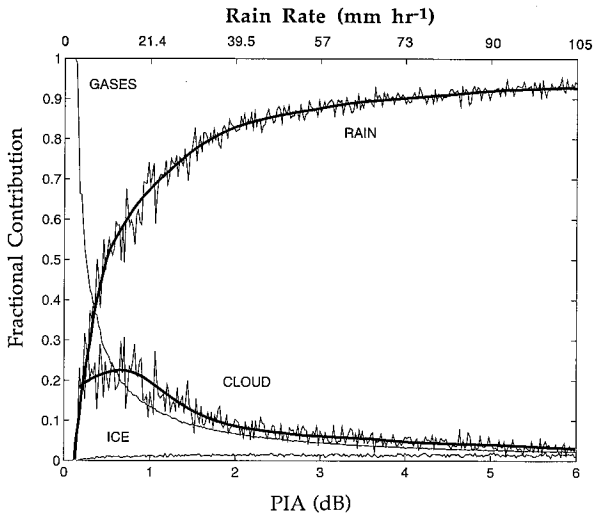

FIG. 7. Percentage of total 13.8-GHz path attenuation contributed by each of four atmospheric sources: (i) active gases (H_2O and O_2), (ii) nonprecipitating cloud water, (iii) rain drops, and (iv) total ice mass. The results are average values from a series of simulations described in section 2 and are not meant to represent all classes and types of precipitation. Smooth fits to the cloud and rain contribution curves are provided to facilitate interpretation. A rain-rate scale is also provided based on the κ–R relationship used in Fig. 4.

(1994b) and Xiang et al. (1994), and that used by Evans et al. (1995). Both models are based on an Eddington plane-parallel two-stream solution to the radiative transfer equation. The models are configured for the four TMI/AMPR frequencies of 10.7, 19, 37, and 85 GHz, and the PR/ARMAR frequency of 13.8 GHz. The Eddington approximation is accepted as a viable option in the microwave spectrum due to the relatively small size parameters of the scattering hydrometeors and its intrinsic computational efficiency essential for inversion-based cloud profiling retrieval algorithms (see Smith et al. 1994a). Applicability of the Eddington approximation for microwave cloud-profiling problems has been discussed by Kummerow (1993), who determined that for realistic layered clouds, the top-of-atmosphere T_B differences derived from the Eddington model and a rigorous eight-stream discrete ordinate model never exceeded 3°C.

The Eddington model requires the vertical profile of temperature $T(z)$, total mass extinction coefficient $\kappa_{\text{ext}}^{\text{tot}}$, total single scatter albedo $\omega^{\text{tot}} = \kappa_{\text{sca}}^{\text{tot}}(\kappa_{\text{abs}}^{\text{tot}} + \kappa_{\text{sca}}^{\text{tot}})^{-1}$, and total asymmetry factor g^{tot} for each layer in the vertical. These quantities are obtained via the standard accumulation and averaging relationships involving interacting components where $\kappa_{\text{ext}}^{\text{tot}} = \kappa_{\text{ext}}^{c} + \kappa_{\text{ext}}^{r} + \kappa_{\text{ext}}^{i} + \kappa_{\text{ext}}^{g}$, $\omega^{\text{tot}} = (\kappa_{\text{ext}}^{r}\omega^{r} + \kappa_{\text{ext}}^{i}\omega^{i})(\kappa_{\text{ext}}^{\text{tot}})^{-1}$, and $g^{\text{tot}} = (\kappa_{\text{ext}}^{r}\omega^{r}g^{r} + \kappa_{\text{ext}}^{i}\omega^{i}g^{i})(\kappa_{\text{ext}}^{\text{tot}}\omega^{\text{tot}})^{-1}$, in which the superscripts c, r, i,

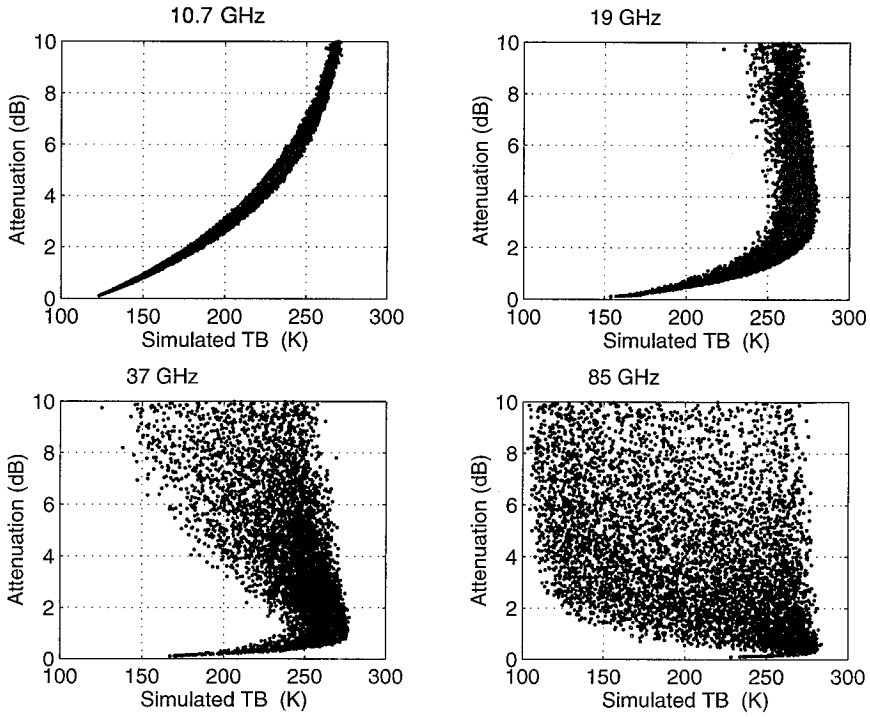

FIG. 8a. Scatter relationships between total path attenuation (dB) at 13.8 GHz to unpolarized brightness temperature (K) for 10.7, 19, 37, and 85 GHz. Results are presented for nadir view. The calculations are made for an SST of 303 K and a U of 20 m s^{-1}.

and g refer to cloud, rain, ice, and absorbing gases, respectively. For each DSD, the above properties for the spherical-shaped rain and ice hydrometeors are obtained using standard Mie theory. Lower-density ice particles such as snow and graupel are simulated using the Lorentz–Lorenz mixing rule. A combined water vapor and oxygen absorption coefficient κ_{abs}^{g} is obtained using Liebe's MPM92 model (Liebe 1985). Nonprecipitating cloud drop–sized hydrometeors are assumed to lie in the Rayleigh regime at all frequencies considered here, where their extinction coefficient $\kappa_{\text{ext}}^{c} = \kappa_{\text{abs}}^{c}$ is independent of DSD, depending only on frequency and temperature. The expression for PIA (dB) at a given frequency is given by the expression $10 \log_{10}\{\exp[\int \beta_{\text{ext}}^{\text{tot}}(z)dz]\} = 4.34 \int \beta_{\text{ext}}^{\text{tot}}(z)dz$, where the volume extinction coefficient $\beta_{\text{ext}}^{\text{tot}}(z) = \rho(z)\kappa_{\text{ext}}^{\text{tot}}(z)$ is determined from the ambient atmospheric density and the integration extends from the sea surface to the top of the T–q profile (~20 km).

Figure 7 provides a summary of the RTE calculations in a diagram that presents the separate fractional contributions to PIA at 13.8 GHz by gases, cloud water, rain water, and ice, as a function of PIA. The high-frequency variations indicate simply that there is underlying variance in the contributions by different constituents to the total path attenuation at a given PIA, particularly with respect to the two liquid components cloud and rain (smoothed versions of these two contribution functions are also shown with thick lines). This diagram is helpful in showing how little ice affects attenuation at 13.8 GHz and how important cloud LWC is at the less intense rain rates. It also shows that by a PIA of 4 dB, rain water completely dominates the total attenuation.

4. RTE modeling results

Scatter diagrams of total path attenuation A/μ, as a function of upwelling brightness temperature at the four TMI window frequencies, are presented in Figs. 8a,b. Here, μ is the cosine of the zenith angle θ of the viewing radiometer. Figure 8a shows the results for the unpolarized nadir view case, whereas Fig. 8b shows results for vertical (VPol) and horizontal (HPol) polarizations at a view angle of 49° (equivalent to a θ of 53° with respect to a spherical earth at TRMM satellite height). Thus, A/μ is the slant-path attenuation and will be henceforth referred to as A when referring to a fixed view angle. The ocean SST is set to 303 K, while the surface wind speed U is set to 20 m s^{-1}. For the imposed variations in cloud, ice, and rain microphysics, the 10.7-GHz T_B's exhibit only small scatter about the mean T_B–A relationship up to a 10-dB slant-path attenuation (equivalent to 6 dB at nadir) for either the unpolarized or polarized case. The higher-frequency 19-GHz T_B's might be useful for estimating path attenuation, but only up to about 1 dB since the relationships become sensitive to the rain and ice DSD variations. Beyond 2 dB,

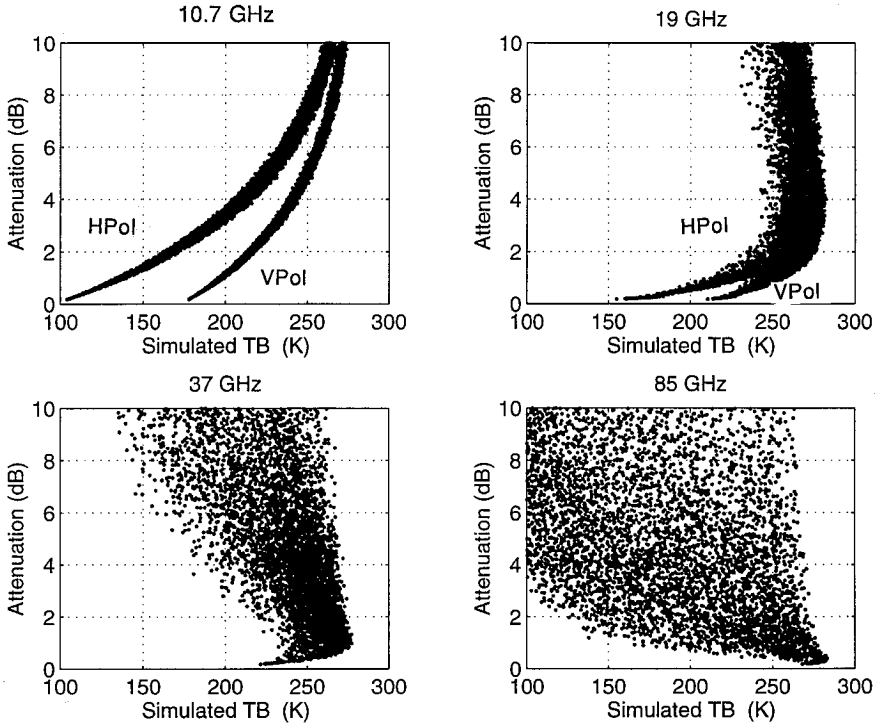

FIG. 8b. Same as Fig. 8a except for the VPol and HPol polarizations associated with a view angle of 49°.

the relationships saturate and render virtually no useful information. At 37 GHz, scattering from ice becomes dominant in controlling the T_B's for path attenuations beyond a fraction of a decibel, and since total atmospheric transmission is so small in precipitating atmospheres at this frequency, the surface becomes virtually obscured to the extent that the VPol and HPol components are indistinguishable. Unlike 19 GHz, dynamic gain is present in the 37-GHz relationships, and unlike 10.7 GHz, which exhibits a positive slope up through A's of 10 dB, the slopes of the 37-GHz relationships go negative just above 1 dB. In the case of 85 GHz, the relationships become so erratic above a fraction of a decibel that physical description is unwarranted. The scatter observed at the two higher frequencies helps illustrate the ambiguities associated with physically based T_B–R relationships that rely on too-simple microphysical parameterizations for hydrometeor DSDs and vertical profiles of nonprecipitating and precipitating water and ice components. The article of Lee (1995) is helpful in examining this issue at even higher microwave frequencies.

Figure 9a shows T_B–A relationships (polarized case) at 10.7 GHz for wind-roughened ocean surfaces taken at wind speeds of 0, 10, 20, and 30 m s^{-1}. As expected, the effect of increasing wind speed is to shift the baseline 0-dB reference level to higher T_B's, especially for horizontal polarization. Although the effect for vertically polarized T_B's is not as obvious, it is detectable. An identical diagram at 19 GHz is presented in Fig. 9b for the region between 0 and 2 dB before saturation occurs. These relationships are not nearly as tight as at 10.7 GHz, although they have the same basic response to variations in surface roughness, with the HPol case showing greatest sensitivity. Note that almost 20°C variations in T_B at a fixed total path attenuation are evident for the clear-sky situations, where only the active gaseous constituents (H_2O and O_2) give rise to attenuation (the region $A < \sim 0.25$ dB). This is indicative of how important variations in the specified vertical structure of moisture are to 19-GHz T_B's when viewing cloud-free columns. Note also that a 0-dB reference is not relevant at this frequency since even for a completely dry and cloud-free atmosphere, oxygen absorption leads to a significant nonzero attenuation (the same can be said for 10.7 GHz, except that the nonzero attenuations for clear, dry atmospheres are minuscule at this frequency). A salient feature of the 19-GHz relationships is that the dynamic ranges are more restricted than at 10.7 GHz (note that the initial abscissa value is 150 K in Fig. 9b, whereas it is 100 K in Fig. 9a). The increased scatter about the general trend is due to an increased dependency on the explicit form of the rain and graupel DSDs, as well as increased radiative contributions from nonprecipitating cloud water. For our purposes, this is unfortunate since the TMI 19-GHz footprint size of 19 km is half that at 10.7 GHz and would make correction for beam filling easier to accommodate. However, 19

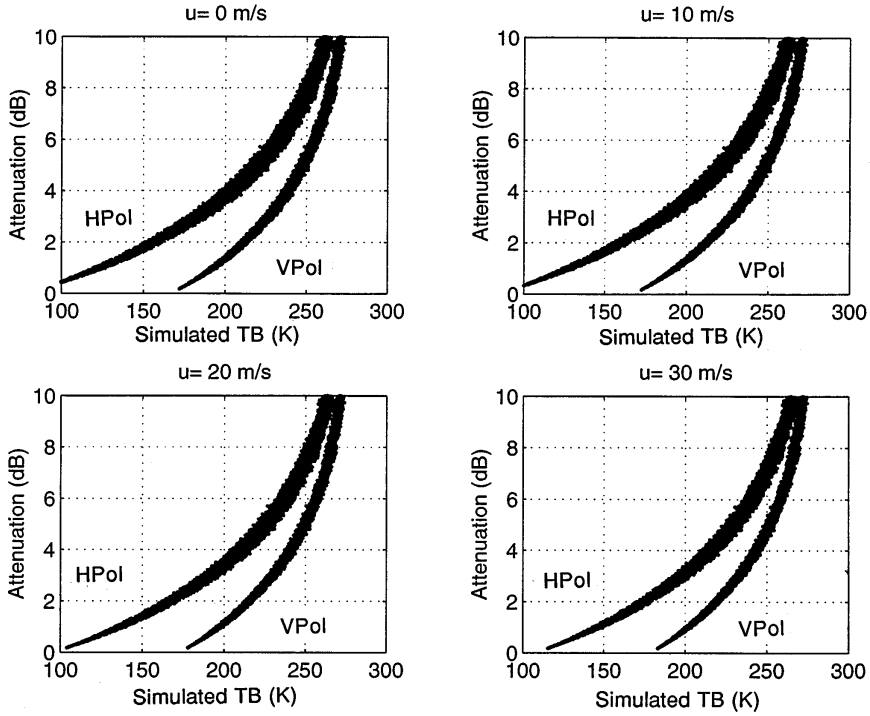

FIG. 9a. Scatter relationships similar to that shown in the 10.7-GHz panel of Fig. 8b except for four different cases of surface wind speed.

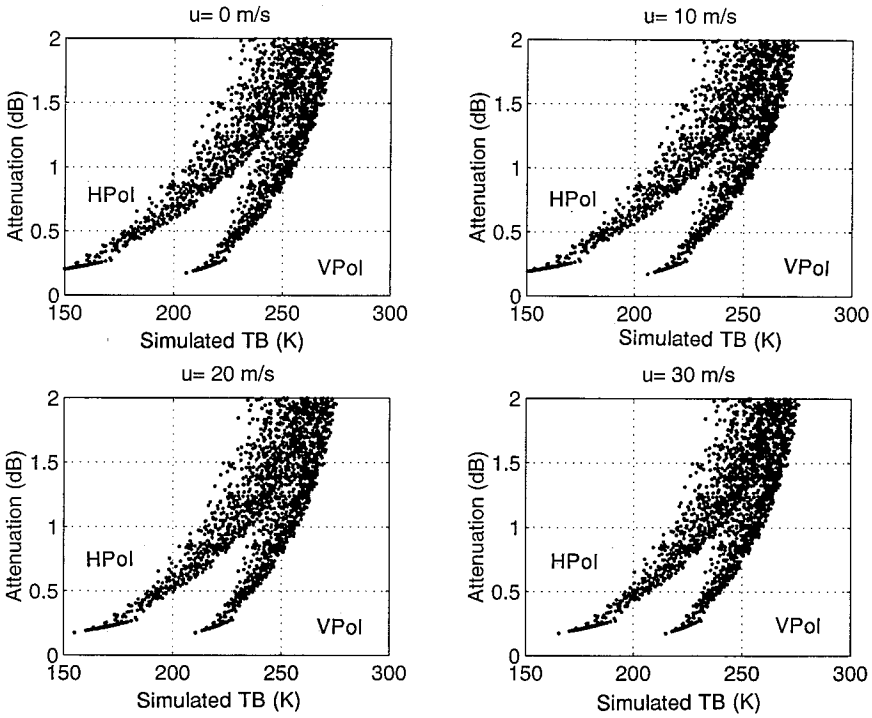

FIG. 9b. Same as Fig. 9a except for 19 GHz.

GHz is simply not a Rayleigh frequency relative to typical precipitating hydrometeor sizes, and as a result, it is an unsatisfactory frequency for trying to characterize total path attenuation over the relevant range.

Based on Fig. 7, one can attribute at least 75% of the total path attenuation above 1 dB to the rain component alone. Hence, it is instructive to consider the rain component path attenuation A_r as a function of brightness temperature, in contrast to total attenuation as depicted in Figs. 8 and 9. Using a diagram format equivalent to that used for Fig. 9, the relationships for 10.7 and 19 GHz for the four cases of a wind-roughened ocean surface are examined. The eight panels (not shown) are similar to those in Fig. 9, except that there is much more scatter. The notable feature in all diagrams is that for any given brightness temperature, there is a range of possible attenuations due to rain that is directly associated with how variances associated with DSDs, wind speeds, cloud-rain water paths, etc. are imposed in the course of the RTE calculations. Therefore, for 10.7 GHz, at the lower T_B range associated with the smaller attenuations (100–150 K), the total rain component attenuations range from 0 to almost 2 dB. As one moves to the right on any of the diagrams, roughly the same total range is considered in the simulations (i.e., ~2 dB), so that the ensemble of attenuation values varying over a 2-dB range simply slides along a curved line representing the underlying mean T_B–A_r relationship. However, since the mean T_B–A_r relationships are exponential, in moving to the larger attenuations, the associated $\Delta A_r/\Delta T_B$ increases while sensitivity decreases. At 19 GHz, again only considering a range of 0 to 2 dB, the distinction between vertical and horizontal polarization becomes quickly obscured as attenuation increases, and any suggestion of a meaningful statistical relationship, such as present in the 10.7-GHz case, is tenuous. This issue is important in attempting to interpret low-frequency brightness temperature information purely in terms of the rain component. The uncertainties are substantial, and although the results we have analyzed are strictly an artifact of how the model imposes variability on constituent hydrometeors and gases that affect the attenuation properties of the atmosphere, they illustrate in a physically germane fashion why rain retrieval from passive microwave measurements alone involves fundamental and impermeable uncertainties that cannot be overcome.

5. Functional relationship between 10.7-GHz T_B's and 13.8-GHz PIAs

The basis for the TRMM day 1 combined radar–radiometer algorithm is a reliable estimate of total path attenuation at 13.8 GHz, the TRMM PR frequency, from the TMI radiometer. This provides PIA estimates independent from the PR reflectivity measurements (i.e., the SRT-based PIAs), thus avoiding synergistic errors from arising when using the PR reflectivities to interpret rain intensities through a presumed DSD formulation. Reflectivities from the PR instrument provide the basic input to the PR module of the TRMM combined algorithm, which in essence is a constrained solution to the Hitschfeld–Bordan (1954) form of the radar equation at multiple range gates (see Iguchi and Meneghini 1994). We will use the V and H T_B's at 10.7 GHz from TMI to estimate 13.8-GHz PIAs, based on the above evidence that the associated attenuations at these two frequencies exhibit a high degree of correlation. The functional relationship derived for this purpose in the remainder of this section constitutes the TMI module to the TRMM day 1 combined algorithm. The radar portion of the algorithm is currently under development at NASA JPL in Pasadena, California, and CRL in Tokyo, Japan (Z. Haddad and T. Iguchi 1995, personal communication), following the approach outlined by Iguchi and Meneghini (1994) and Haddad et al. (1996b).

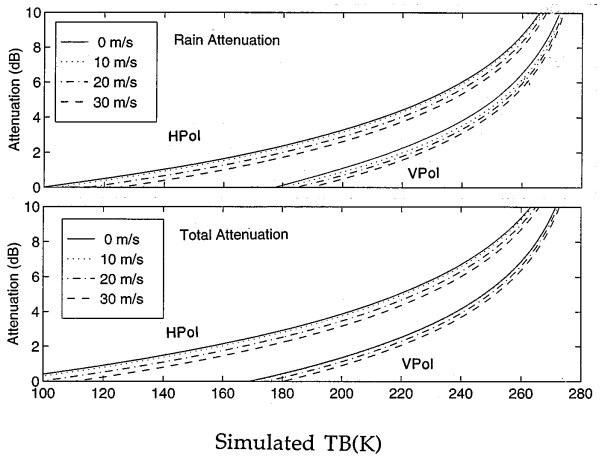

FIG. 10. Functional relationships (statistical best fits) between rain component path attenuation (top panel) and total path attenuation (dB) (bottom panel) at 13.8 GHz to 10.7-GHz brightness temperature (K). Results are presented for both VPol and HPol. The calculations are done at an SST of 303 K; functional relationships are expressed at four different surface wind speeds.

Weinman et al. (1990) proposed a relationship of the form $A/\mu = a + b \ln(T_o - T_B)$ for expressing the generally log-linear relationship of attenuation at 10.7 GHz to brightness temperature at the same frequency. This formulation was also used by Durden et al. (1995) at 13.8 GHz in an analysis of simultaneously acquired radar and radiometer measurements from the ARMAR instrument. Obtaining T_o and the a and b coefficients from modeled A's and T_B's requires a regression procedure that determines the value of T_o yielding the best-fit straight line to a linked distribution of A/μ's and $\ln(T_o - T_B)$'s. The 0-db reference level T_{ref} is given by $T_o - \exp(-a/b)$.

Using this formulation, Fig. 10 shows graphs of 13.8-GHz rain component and total path attenuations (A_r/μ and A/μ on the ordinates) as functions of 10.7-GHz T_B (on the abscissas). Results are given for both vertical

TABLE 5. Coefficients in relationship $A = a + b \ln(T_o - T_B)$, where A is the 13.8-GHz path attenuation (dB), T_B is the 10.7-GHz T_B, and T_{ref} is the 0-dB reference level brightness temperature (note that $T_o > T_B > T_{ref}$). Coefficients are given for 49° view polarized case and nadir view unpolarized case. These coefficients are fit to calculations over the entire range of U's indicated in Table 4, but for a fixed SST of 303 K.

	a	b	T_o	T_{ref}
Vertical polarization (49° view)	20.0438	−4.2470	282.03	169.92
Horizontal polarization (49° view)	22.8144	−4.3401	283.28	91.44
Both polarizations (0° view)	21.8605	−4.2860	285.87	121.78

and horizontal polarizations; the calculations assume an SST of 303 K. The upper panel shows the rain component attenuation, while the lower panel shows the PIA. Each panel contains results for four different wind speeds. As discussed, surface wind essentially determines the value of the baseline T_B, with the most noticeable differences in an attenuation relationship occurring between 10 and 30 m s^{-1}. A decrease in SST from 303 to 293 K (not shown) has a less significant but detectable effect—to lower the T_B's slightly for a given path attenuation. Also of note is that the vertically polarized T_B's are slightly less dependent upon surface wind speed variations. By the same token, the dynamic range of vertically polarized T_B's is less than that of the horizontally polarized T_B's.

Table 5 gives values of a, b, T_o, and T_{ref} for 10.7-T_B–13.8-GHz PIA relationships considering the range of variation for U given in Table 4, but at a fixed SST of 303 K. Results are presented for vertical and horizontal polarizations at a 49° view angle and for an unpolarized nadir view where $T_B^V = T_B^H$. Note that the differences in the a and b coefficients for the three cases are relatively small, and yet because the form of the relationship is logarithmic, slight differences in the a and b coefficients lead to large differences in T_{ref}. Put another way, the dynamic range expressed in the relationship is very sensitive to the chosen values of a and b. This simply points to the care that must be taken in fitting the distributions of A's and T_B's resulting from the simulations to preserve the relationships intrinsic to the simulations.

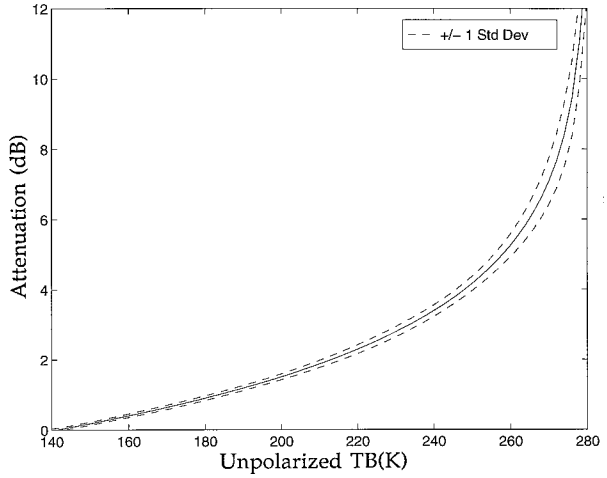

FIG. 11. Functional relationship between PIA at PR radar zenith angle of 0° (nadir), with respect to 10.7-GHz unpolarized T_B measured at a TMI view angle of 49°. The plus/minus one-sigma lines of PIA are indicated by dashed lines. This functional relationship represents a best fit to the RTE calculations using all possible variations of cloud–rain–ice parameters, surface conditions, and atmospheric profiles as described in Table 4.

Examination of daily ship reports from vessels deployed in the TOGA COARE study area indicates that SSTs varied between 301 and 304 K, while surface wind speeds were typically on the order of 5–10 m s^{-1} (TCI-PO Staff 1993). Therefore, it is reasonable to derive an overall T_B–A relationship that takes into consideration the expected variations in SST and U. This type of relationship is preferable for the operational TRMM algorithm because direct access to accurate values of these quantities will not necessarily be available. In generating this more general form of the relationship, we pay particular attention to the variance about the best-fit line since the variance represents the underlying uncertainty in estimating A at 13.8 GHz from a T_B at 10.7 GHz. This is a critical parameter for the combined algorithm since conditional probabilities from application of the Bayesian theorem are used to adjust weights on initial multiple solutions to the radar equation over a specified DSD domain, based on proximities of the radar-determined PIAs to the plus/minus one-sigma PIA region defined by the given 10.7 T_B (sigma being the standard deviation of PIA at a given T_B). The justification of a statistical aggregation approach is explained in the study of Haddad et al. (1996b). In essence, if the mean and variance parameters of the radiometer-based PIA estimates are accurately specified, the unadjusted (initial) radar solutions are simply that much better corrected by the radiometer information.

One realization of the function developed for the day 1 TRMM combined algorithm for the range of atmosphere and surface conditions described in Table 4 is graphed in Fig. 11. The diagram gives A/μ_r at 13.8 GHz on the ordinate versus T_B at 10.7 GHz on the abscissa (assuming a TMI view angle of 49°). Here, μ_r is the cosine of the radar zenith angle θ_r. (Note for small view angles over a sphere, view angle and zenith angle are nearly synonymous). The plus/minus one standard deviation lines (dashed) of the PIAs with respect to T_B are also drawn. Similar relationships (not shown) calculated out to a radar view angle of 17° (conforming to the PR scan limit) exhibit detectable but minor differences. It

is evident from these diagrams that the spread of the variance reaches maximum values between 4 and 6 dB, generally diminishing for larger values of attenuation. It is also clear from the complete set of calculations that dynamic range improves at the high attenuation range and variance decreases as the radar view angle increases. It is presumed that these improvements in the attenuation relationship as radar view angle increases will partially compensate for the uncertainty in the rain retrievals due to the corresponding loss of sensitivity in the radar measurements as the radar scans away from nadir.

6. Examination of PR–TMI differences in viewing geometry and resolution

An important issue associated with the viewing geometry is the fact that the TMI and PR will view earth scenes from different geometric perspectives and at substantially different ground resolutions since the 10.7-GHz TMI beam size is 10 times that of the radar beam size (see Table 1). Moreover, because the TMI is forward viewing while the PR scans through nadir, there will be almost a 1-min difference in time before the PR beam passes over a scene already observed by the TMI. During 1 min the microphysical nature and structure of a rain cloud will evolve, in addition to its undergoing horizontal translation due to advection. In most cases such changes will be small, but not always. There are no straightforward means to resolve the differences brought on by the noncoincident viewing, dissimilar spatial resolutions, and staggered sampling times; thus uncertainties in any type of combined radar–radiometer algorithm will arise. Moreover, such uncertainties will not be thoroughly understood until TRMM data are available and the combined algorithm can be thoroughly exercised.

Although the TMI view angle will be fixed at 49° and the PR scan angle limited to a 0°–17° range for reasons specific to the individual instruments, it is worth exploring the properties of the T_B–PIA relationship as the radiometer view angle varies in conjunction with variations in the radar view angle to help understand the strengths and weaknesses of noncoincident viewing geometry. The T_B–PIA computer subroutine developed for the combined algorithm has been designed so that both radiometer and radar view angle are variable parameters.[1] Figure 12 shows two sets of scatter diagrams involving all 10 000 RTE calculations in which three radar view angles are considered (0°, 20°, and 49°) for two different radiometer view angles, the first taken at nadir (left panels) and the second at 49° (right panels). Three properties are of interest in the T_B–PIA relationships: 1) linearity, 2) dynamic range, and 3) variance magnitude. Linearity is a measure of the slope invariance, while dynamic range is a measure of the slope itself, with a slope angle of 45° representing the optimal dynamic range.

It is clear from these diagrams that as radiometer view angle increases, both linearity and dynamic range fall off, while as radar view angle increases, linearity and dynamic range improve. Alternatively, variance increases with increased radar view angle, simply due to the spread in A produced by $1/\mu_r < 1$, and decreases with increased radiometer view angle because the same attenuation interval is distributed over a larger T_B interval (i.e., the longer T_B path stretches the function and tightens the point spread). Over a radar view angle of 0°–20°, variance is virtually unaffected. Of note is the fact that the radiometer view angle represents the stronger control on variance, and in this regard the 49° conical-scan radiometer view angle is preferable over a nadir view. By the same token, the decreased linearity and loss of dynamic range at high attenuations for the 49° view angle, particularly in conjunction with small radar view angles, represents a shortcoming in the TMI–PR viewing configuration.

It is not surprising that the ideal configuration for optimizing linearity and dynamic range while reducing variance comes from matching the radiometer view angle with that of the radar (evident from the Fig. 12 diagram). This also produces the preferred time coincidence. The problem with such a solution is that for a coincident cross-track scanning configuration extended to ''wide swath'' the radiometer and radar paths become unwieldy at large view angles, and the changing path complicates interpretation of the radiometer T_B because it is a total path, not a pulsed measurement. Alternatively, for coincident fixed-path conical scanning, which is optimal for radiometer purposes, the radar would lose sensitivity at higher attenuations compared to the relatively small viewing angles of a restricted cross-track scanner, such as that used for the PR. Obviously, the physics of path effects on radiometer- and radar-type measurements are not easily resolved, an issue complicating combined retrieval.

While we have emphasized the utility of the TMI for complementing the PR reflectivity measurements for estimating the vertical profile of rain, the PR measurements can be used in a complementary fashion to account for the variable dimensions and intensities of rain cells within the much larger 10.7-GHz beams. Near nadir, approximately 100 radar beams are contained inside any given TMI 10.7-GHz footprint. Using the SRT-constraint method to estimate the path-averaged rain rate along each beam, a threshold can be set in order to determine to first order whether the beam intercepts precipitation or not. This obviously involves accurate coregistration of the radar and radiometer beams. Once coregistration is achieved, the PR-only-derived rain rates and rain area can be used in adjusting the TMI-derived attenuation for heterogeneous beam filling effects. Since the T_B–A relationship is nonlinear, variations

[1] A copy of the computer code is available from the authors.

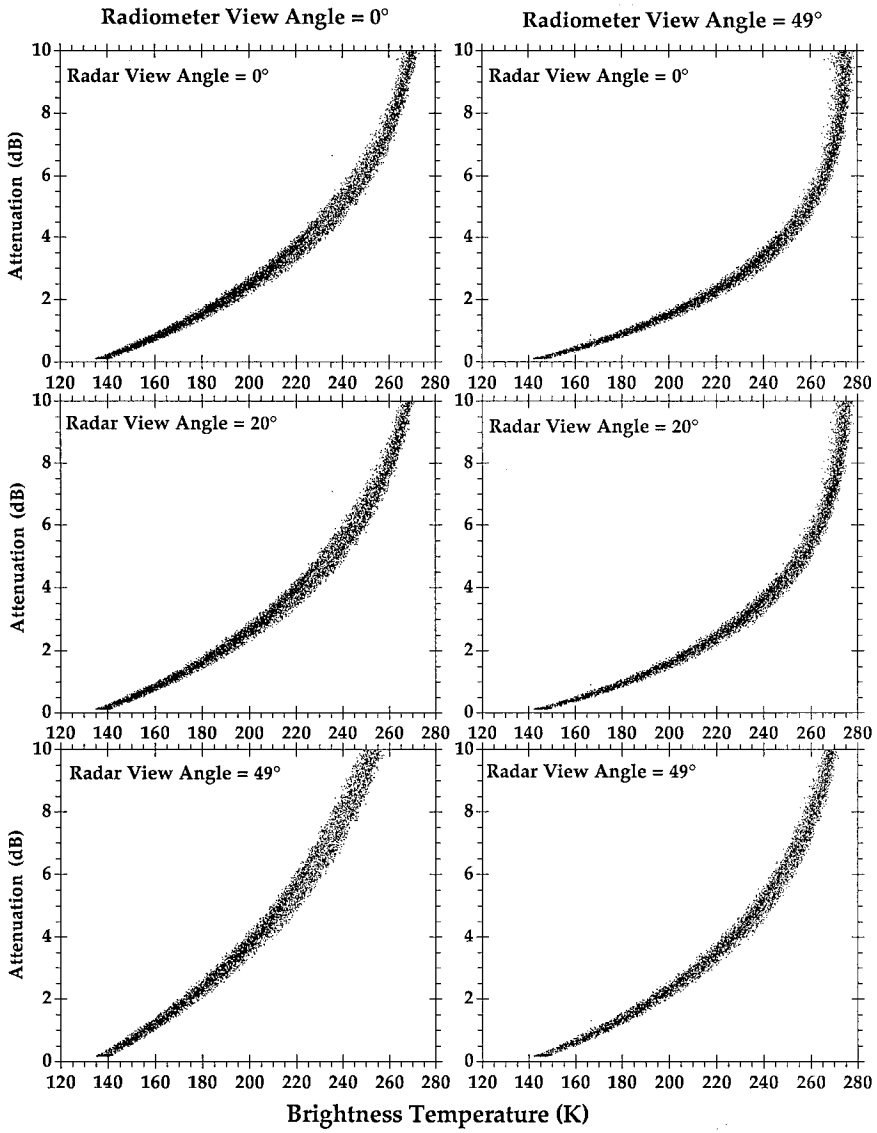

FIG. 12. Scatter diagrams based on 10 000 RTE calculations between radiometer-based 10.7-GHz T_B's taken at 0° (left panels) and 49° (right panels) and radar-based 13.8-GHz PIAs considered at three different view angles: (i) top panels are 0° cases, (ii) middle panels are 20° cases, and (iii) bottom panels are 49° cases.

in A across a single footprint cannot be accounted for with a single beam-averaged T_B—that is, $\overline{A} = f(\overline{T}_{Bi}) \neq \overline{f}(T_{Bi})$. However, it is possible to formulate a correction factor χ for $\overline{A}$ related to the rain cover a_r, mean rain intensity $\overline{\eta}(R_i)$, and variance of rain intensity $\gamma(R_i)$ within the beam—that is, $\overline{A}' = \chi[a_r, \overline{\eta}(R_i), \gamma(R_i)]\overline{A}$. This issue is currently under study. It should be noted that this correction scheme eschews the uncertainty due to nonuniform beam filling within the PR footprint (see Nakamura 1991; Amayenc et al. 1993), although progress has been made by Kozu and Iguchi (1995) in relating the variance of rain rate within a single radar beam to the variance of beam-averaged rain rates over a localized set of beams surrounding the single beam.

As noted in Table 1, the PR swath is less than one-third of that of the TMI (220–760 km). Therefore, a combined algorithm can only be invoked physically within the ''narrow'' radar swath. Formulating a combined algorithm across the entire TMI swath means statistically adjusting some type of TMI result across the wide swath by a factor obtained from differences between the combined algorithm and the TMI algorithm within the narrow swath. This approach presumes the combined algorithm provides a more accurate rain estimate than the TMI algorithm but that the retrieved vertical structures from the two algorithms are somewhat synonymous. Thus, the correction is strictly an adjustment for bias. Such a scheme is included as part

of the day 1 TRMM combined algorithm. The day 1 TMI vertical profile algorithm described by Wilheit (1995) will be used with the combined algorithm for this purpose. Various algorithms being used with SSM/I measurements have already demonstrated sensitivity to microphysical vertical structure (see Smith et al. 1994b; Smith et al. 1995a; Kummerow and Giglio 1994a,b; Evans et al. 1995; and Pierdicca et al. 1996).

7. Conclusions

The use of radiometer T_B's at 10.7 GHz to infer 13.8-GHz PIAs has been demonstrated. The application is linked to the day 1 TRMM combined radar–radiometer precipitation retrieval algorithm. Combined algorithms are expected to provide improved retrievals of rain vertical structure over the open ocean and, thus, improved estimates of latent heat release and the time–space distribution of diabatic heating in the Tropics. Such improvements would be of direct benefit to the climatological description of rainfall, to interpretation of the general circulation, and to physical initialization of numerical prediction models, as suggested by the formative SSM/I studies of Chang and Holt (1991, 1994) (see also Krishnamurti et al. 1993).

The main advantages of the radiometer-based approach are its independence from the radar measurements, its ease of implementation, and its relatively stable variance properties (compared to the radar-based SRT). Based on the analysis at the TMI–PR viewing geometry, the dynamic range properties of the T_B–PIA functional relationship are tractable out to total path attenuations of about 8 dB. Analyses of higher frequencies used for developing such T_B–PIA relationships demonstrate that with the exception of a limited range of attenuation up to perhaps 1 dB predictable with 19-GHz T_B's, the 10.7-GHz frequency T_B is the appropriate TMI measurement to provide an independent estimate of PIA. Clearly, further investigation of how much improvement can be gained by using radiometer-derived attenuation over SRT-derived attenuation is needed once TRMM is launched.

As evident from Table 1, since the viewing geometries of the PR and TMI instruments are not coincident and the ground resolution of the diffraction-limited 10.7-GHz TMI radiometer beam is about 100 times larger than that of the PR beam, there will be difficulties in realizing the potential improvement offered by the combined approach. Furthermore, because the TMI is forward viewing at 49° while the PR is nadir viewing, the respective measurements will be displaced nearly 1 min in time, during which the underlying rain microphysics will change. Nevertheless, various steps that can be taken to mitigate problems with beam size differences have been discussed, and quantitative arguments have been offered concerning why the noncoincident PR–TMI viewing geometry being used for TRMM is preferable over a bore-sighted approach.

Continual testing prior to the launch of the TRMM satellite will be carried out using the coordinated ARMAR–AMPR measurements obtained during TOGA COARE to better understand the problematic issues and to refine the combined algorithm procedures. Although these tests are not a true substitute for TRMM-based tests, they will help shed light on how uncertainties in rain retrieval are related to microphysical conditions and errors intrinsic to total path attenuation estimates. More substantive tests will be conducted after the TRMM launch. It will be at that time that the true merit of a combined algorithm can be evaluated against the single-instrument PR and TMI algorithms. Although substantial improvement may not be immediate because of the incongruities in the measurements, the improved physical framework of the scheme bodes well for an advanced generation of physically based satellite retrieval algorithms.

Acknowledgments. The authors express their appreciation to Ms. Robbie Hood, Mr. Frank LaFontaine, and Dr. Roy Spencer of the NASA Marshall Space Flight Center for providing the AMPR data, and to Dr. Steve Durden of the NASA Jet Propulsion Laboratory for providing the ARMAR data and its access software. We also wish to thank Dr. Frank Evans of the University of Colorado, who provided his radiative transfer model for parts of the RTE calculations; Dr. Grant Petty of Purdue University, who provided his ocean surface emissivity model; and Drs. Ziad Haddad, Toshio Iguchi, Christian Kummerow, and Joanne Simpson, who provided fruitful discussion in the course of the research. The first author extends his appreciation to Drs. Simon Chang and Jeffrey Hawkins of the Naval Research Laboratory in Monterey, California, for providing facilities under their visiting scientist program while this paper was being prepared. Mr. Brian Swilling's assistance in computer graphics support is gratefully acknowledged. The research at The Florida State University has been supported under NASA Grants NG5-2672 and NAGW-3970. Joseph Turk was supported at Colorado State University under NASA Grant NAG8-890, and he acknowledges the current sponsorship of the Space and Naval Warfare Systems Command, Program Element 0602435N. A portion of the computing resources has been provided by the Supercomputer Computation Research Institute at The Florida State University under U.S. Department of Energy Contract DOE-FC05-85ER250000.

REFERENCES

Amayenc, P., M. Marzoug, and J. Testud, 1993: Analysis of cross-beam resolution effects in rainfall rate profile retrieval from a spaceborne radar. *IEEE Trans. Geosci. Remote Sens.*, **31,** 417–425.

Andrieu, H., and J. D. Creutin, 1995: Identification of vertical profiles of radar reflectivity for hydrological applications using an in-

verse method. Part I: Formulation. *J. Appl. Meteor.,* **34,** 225–239.

Atlas, D., 1994: Footprints of storms on the sea: A view from spaceborne synthetic aperature radar. *J. Geophys. Res.,* **99,** 7961–7969.

Awaka, J., T. Kozu, and K. Okamoto, 1988: A feasibility study of rain radar for the Tropical Rainfall Measuring Mission. Part 2: Determination of basic system parameters. *J. Comm. Res. Lab.,* **35,** 111–133.

CalVal, 1989: DMSP Special Sensor Microwave/Imager calibration/validation. CalVal Final Report. [Available from Naval Research Laboratory, Washington, DC, 20375–5000.]

Chang, S. W., and T. R. Holt, 1991: Impact of SSM/I rainfall rates on numerical prediction of cyclones. Preprints, *First Int. Symposium on Winter Storms,* New Orleans, LA, Amer. Meteor. Soc., 151–153.

——, and ——, 1994: Impact of assimilating SSM/I rainfall rates on numerical prediction of winter cyclones. *Mon. Wea. Rev.,* **122,** 151–164.

Durden, S. L., E. Im, F. K. Li, W. Ricketts, A. Tanner, and W. Wilson, 1994: ARMAR: An airborne rain mapping radar. *J. Atmos. Oceanic Technol.,* **11,** 727–737.

——, Z. S. Haddad, E. Im, A. Kitiyakara, F. K. Li, A. B. Tanner, and W. J. Wilson, 1995: Measurement of rainfall path attenuation near nadir: A comparison of radar and radiometer methods at 13.8 GHz. *Radio Sci.,* **30,** 943–947.

Evans, K. F., and J. Vivekanandan, 1990: Multiparameter radar and microwave radiative transfer modeling of nonspherical atmospheric ice particles. *IEEE Trans. Geosci. Remote Sens.,* **28,** 423–437.

——, J. Turk, T. Wong, and G. L. Stephens, 1995: A Bayesian approach to microwave precipitation profile retrieval. *J. Appl. Meteor.,* **34,** 260–279.

Farrar, M. R., and E. A. Smith, 1992: Spatial resolution enhancement of terrestrial features using deconvolved SSM/I microwave brightness temperatures. *IEEE Trans. Geosci. Remote Sens.,* **30,** 349–355.

——, ——, and X. Xiang, 1994: The impact of spatial resolution enhancement of SSM/I microwave brightness temperatures on rainfall retrieval algorithms. *J. Appl. Meteor.,* **33,** 313—333.

——, ——, and ——, 1996: Combined radar–radiometer precipitation retrieval for TRMM. Part II: The retrieval algorithm. Preprints, *Eighth Conf. on Satellite Meteorology and Oceanography,* Atlanta, GA, Amer. Meteor. Soc., 259–260.

Fujita, M., K. Okamoto, H. Masuko, T. Ojima, and N. Fugono, 1985a: Quantitative measurements of path-integrated rain rate by an airborne microwave radiometer over ocean. *J. Atmos. Oceanic Technol.,* **2,** 285–292.

——, ——, S. Yoshikado, and K. Nakamura, 1985b: Inference of rain rate profile and path-integrated rain rate by an airborne microwave rain scatterometer. *Radio Sci.,* **20,** 631–642.

Haddad, Z. S., A. R. Jameson, E. Im, and S. L. Durden, 1995: Improved coupled *Z–R* and *k–R* relations and the resulting ambiguities in the determination of the vertical distribution of rain from the radar backscatter and the integrated attenuation. *J. Appl. Meteor.,* **34,** 2680–2688.

——, S. L. Durden, and E. Im, 1996a: Parameterizing the raindrop size distribution. *J. Appl. Meteor.,* **35,** 3–13.

——, E. Im, S. L. Durden, and S. Hensley, 1996b: Stochastic filtering of rain profiles using radar, surface-referenced radar, or combined radar–radiometer measurements. *J. Appl. Meteor.,* **35,** 229–242.

Hai, L., X. Miaoxin, W. Chong, H. Yaokui, and Z. Shouxiang, 1985: Ground-based remote sensing of LWC in cloud and rainfall by a combined dual-wavelength radar–radiometer system. *Adv. Atmos. Sci.,* **2,** 93–103.

Hitschfeld, W., and J. Bordan, 1954: Errors inherent in the radar measurement of rainfall at attenuating wavelengths. *J. Meteor.,* **11,** 58–67.

Hogg, D. C., 1989: Rain, radiometry, and radar. *IEEE Trans. Geosci. Remote Sens.,* **27,** 576–585.

Iguchi, T., and R. Meneghini, 1994: Intercomparison of single-frequency methods for retrieving a vertical rain profile from airborne or spaceborne radar data. *J. Atmos. Oceanic Technol.,* **11,** 1507–1511.

Jameson, A. R., 1991: The effect of drop-size distribution variability on radiometric estimates of rainfall rates for frequencies from 3 to 10 GHz. *J. Appl. Meteor.,* **30,** 1025–1033.

Janssen, M. A., 1993: An introduction to the passive microwave remote sensing of atmospheres. *Atmospheric Remote Sensing by Microwave Radiometry,* M. A. Janssen, Ed., John Wiley & Sons, 1–35.

Klein, L. A., and C. T. Swift, 1977: An improved model for the dielectric constant of sea water at microwave frequencies. *IEEE Trans. Geosci. Remote Sens.,* **25,** 104–111.

Kozu, T., and K. Nakamura, 1991: Rainfall parameter estimation from dual-radar measurements combining reflectivity profile and path-integrated attenuation. *J. Atmos. Oceanic. Technol.,* **8,** 259–270.

——, and T. Iguchi, 1995: Nonuniform beam filling correction for spaceborne radar rainfall retrieval. Preprints, *27th Conf. on Radar Meteorology,* Vail, CO, Amer. Meteor. Soc., 797–799.

——, K. Nakamura, R. Meneghini, and W. C. Boncyk, 1991: Dual-parameter radar rainfall measurement from space: A test result from an aircraft experiment. *IEEE Trans. Geosci. Remote Sens.,* **29,** 584–592.

Krishnamurti, T. N., H. S. Bedi, and K. Ingles, 1993: Physical initialization using SSM/I rain rates. *Tellus,* **45A,** 247–269.

Kumagai, H., M. Thurai, and J. R. Wang, 1993a: Precipitation profiling using single-frequency radar and multi-frequency radiometer data obtained from an aircraft experiment. *Proc. 1993 Int. Geoscience and Remote Sensing Symp. (IGARSS '93),* Tokyo, Japan, IEEE/GRSS, 826–828.

——, R. Meneghini, and T. Kozu, 1993b: Preliminary results from multiparameter airborne rain radar measurement in the western Pacific. *J. Appl. Meteor.,* **32,** 431–440.

Kummerow, C., 1993: On the accuracy of the Eddington approximation for radiative transfer in the microwave frequencies. *J. Geophys. Res.,* **98,** 2757–2765.

——, and L. Giglio, 1994a: A passive microwave technique for estimating rainfall and vertical structure information from space. Part I: Algorithm description. *J. Appl. Meteor.,* **33,** 3–18.

——, and ——, 1994b: A passive microwave technique for estimating rainfall and vertical structure information from space. Part II: Applications to SSM/I data. *J. Appl. Meteor.,* **33,** 19–34.

Lee, T. F., 1995: Images of precipitation signatures from DMSP SSM/T2, SSM/I, and OLS. *J. Appl. Meteor.,* **34,** 788–793.

Lhermite, R. M., 1988: Cloud and precipitation remote sensing at 94 GHz. *IEEE Trans. Geosci. Remote Sens.,* **26,** 207–216.

Liebe, H. J., 1985: An updated model for millimeter wave propagation in moist air. *Radio Sci.,* **20,** 1069–1089.

Lu, D., and L. Hai, 1980: Comparisons of radar and microwave radiometer in precipitation measurements and their combined use (in Chinese). *Acta Atmos. Sin.,* **1,** 30–39.

Marzano, F. S., A. Mugnai, E. A. Smith, X. Xiang, J. E. Turk, and J. Vivekanandan, 1994: Active and passive remote sensing of precipitation storms during CaPE. Part II: Intercomparison of precipitation retrievals from AMPR radiometer and CP-2 radar. *Meteor. Atmos. Phys.,* **54,** 29–52.

——, J. Turk, S. Dietrich, A. Mugnai, G. Pannegrossi, N. Pierdicca, and E. A. Smith, 1995: Microwave multisensor rainfall retrieval applied to TOGA–COARE observations. *Proc. 1995 Int. Geoscience and Remote Sensing Symp. (IGARSS '95),* Firenze, Italy IEEE/GRSS, 1895–1897.

Marzoug, M., and P. Amayenc, 1991: Improved range profiling algorithm of rainfall rate from a spaceborne radar with path-integrated attenuation constraint. *IEEE Trans. Geosci. Remote Sens.,* **29,** 584–592.

Meneghini, R., and T. Kozu, 1990: *Spaceborne Weather Radar*. Artech House, 199 pp.

——, and K. Nakamura, 1990: Range profiling of the rain rate by airborne weather radar. *Remote Sens. Environ.,* **31,** 193–209.

——, and J. J. Jones, 1993: An approach to estimate the aerial rain-

rate distribution from spaceborne radar by the use of multiple thresholds. *J. Appl. Meteor.*, **32,** 386–398.

——, J. Eckerman, and D. Atlas, 1983: Determination of rain rate from a spaceborne radar technique. *IEEE Trans. Geosci. Remote Sens.*, **21,** 34–43.

——, A. Jones, and L. H. Gesell, 1987: Analysis of dual-wavelength surface reference radar technique. *IEEE Trans. Geosci. Remote Sens.*, **25,** 456–471.

——, K. Nakamura, C. W. Ulbrich, and D. Atlas, 1989: Experimental tests of methods for the measurement of rainfall rate using an airborne dual-wavelength radar. *J. Atmos. Oceanic Technol.,* **6,** 637–651.

——, T. Kozu, H. Kumagai, and W. C. Boncyk, 1992: A study of rain estimation methods from space using dual-wavelength radar measurements at near-nadir incidence over ocean. *J. Atmos. Oceanic Technol.,* **9,** 364–382.

——, J. R. Wang, H. Kumagai, and T. Iguchi, 1994: Description of a radar/radiometer method and its application to airborne measurements over stratiform rain. *Proc. 1994 International Geoscience and Remote Sensing Symposium (IGARSS '94)*, Pasadena, CA, IEEE/GRSS, 1773–1775.

Mugnai, A., E. A. Smith, and G. J. Tripoli, 1993: Foundations for statistical–physical precipitation retrieval from passive microwave satellite measurements. Part II: Emission source and generalized weighting function properties of a time-dependent cloud-radiation model. *J. Appl. Meteor.*, **32,** 17–39.

Nakamura, K., 1991: Biases of rain retrieval algorithms for spaceborne radar caused by nonuniformity of rain. *J. Atmos. Oceanic Technol.,* **8,** 363–373.

——, K. Okamoto, T. Ihara, J. Awaka, and T. Kozu, 1990: Conceptual design of rain radar for the Tropical Rainfall Measuring Mission. *Int. J. Sat. Comm.*, **8,** 257–268.

Okamoto, K., S. Yoshikado, H. Masuko, T. Ojima, N. Fugono, K. Nakamura, J. Awaka, and H. Inomata, 1982: Airborne microwave rain scatterometer-radiometer. *Int. J. Remote Sens.*, **3,** 277–294.

——, J. Awaka, and T. Kozu, 1988: A feasibility study of rain radar for the Tropical Rainfall Measuring Mission. 6: A case study of rain radar system. *J. Comm. Res. Lab.*, **35,** 183–208.

——, T. Ihara, T. Kozu, N. Nakamura, J. Awaka, and M. Fujita, 1991: Development status of rain radar in the tropical rainfall measuring mission. Preprints, *25th Conf. on Radar Meteorology,* Paris, France, Amer. Meteor. Soc., 388–391.

Olsen, R. L., D. V. Rogers, and D. B. Hodge, 1978: The aR^b relationship in the calculation of rain attenuation. *IEEE Trans. Antennas Propag.*, **26,** 318–329.

Olson, W. S., and C. D. Kummerow, 1995: Passive and active microwave retrievals of precipitation profiles in TOGA COARE and CAMEX. Preprints, *21st Conf. on Hurricanes and Tropical Meteorology,* Miami, FL, Amer. Meteor. Soc., 425–427.

Petty, G., and K. Katsaros, 1994: The response of the SSM/I to the marine environment. Part II: A parameterization of the effect of the sea surface slope distribution on emission and reflection. *J. Atmos. Oceanic Technol.*, **11,** 617–628.

Pierdicca, N., F. S. Marzano, G. D'Auria, P. Basili, P. Ciotti, and A. Mugnai, 1996: Precipitation retrieval from spaceborne microwave radiometers based on maximum a posteriori probability estimation. *IEEE Trans. Geosci. Remote Sens.*, **34,** 1–16.

Robinson, W., C. Kummerow, and W. S. Olson, 1992: A technique for matching the resolution of microwave measurements from the SSM/I instrument. *IEEE Trans. Geosci. Remote Sens.*, **30,** 419–424.

Savage, R. C., and J. A. Weinman, 1975: Preliminary calculations of the upwelling radiance from rain clouds at 37.0 and 19.35 GHz. *Bull. Amer. Meteor. Soc.*, **56,** 1272–1274.

Schols, J. L., and J. A. Weinman, 1994: Retrieval of hydrometeor distributions over the ocean from airborne single-frequency radar and multi-frequency radiometric measurements. *Atmos. Res.*, **34,** 329–346.

Simpson, J., R. F. Adler, and G. North, 1988: A proposed Tropical Rainfall Measuring Mission (TRMM) satellite. *Bull. Amer. Meteor. Soc.*, **69,** 278–295.

——, C. Kummerow, W.-K. Tao, and R. F. Adler, 1996: On the Tropical Rainfall Measuring Mission (TRMM) satellite. *Meteor. Atmos. Phys.*, **60,** 19–36.

Smith, E. A., 1995: Combined TRMM instruments team. *TRMM Science Operations Plan,* J. Simson and C. Kummerow, Eds., NASA Goddard Space Flight Center, 25–29.

——, and A. Mugnai, 1988: Radiative transfer to space through a precipitating cloud at multiple microwave frequencies. Part II: Results and analysis. *J. Appl. Meteor.*, **27,** 1074–1091.

——, ——, H. J. Cooper, G. J. Tripoli, and X. Xiang, 1992: Foundations for statistical–physical precipitation retrieval from passive microwave satellite measurements. Part I: Brightness temperature properties of a time-dependent cloud-radiation model. *J. Appl. Meteor.*, **31,** 506–531.

——, C. Kummerow, and A. Mugnai, 1994a: The emergence of inversion-type precipitation profile algorithms for estimation of precipitation from satellite microwave measurements. *Remote Sens. Rev.*, **11,** 211–242.

——, X. Xiang, A. Mugnai, and G. J. Tripoli, 1994b: Design of an inversion-based precipitation profile retrieval algorithm using an explicit cloud model for initial guess microphysics. *Meteor. Atmos. Phys.*, **54,** 53–78.

——, ——, ——, R. Hood, and R. W. Spencer, 1994c: Behavior of an inversion-based precipitation retrieval algorithm with high-resolution AMPR measurements including a low-frequency 10.7-GHz channel. *J. Atmos. Oceanic Technol.*, **11,** 858–873.

——, A. Mugnai, and G. Tripoli, 1995a: Theoretical foundations and verification of a multispectral, inversion-type microwave precipitation profile retrieval algorithm. *Proc. ESA/NASA Int. Workshop on Microwave Radiometry,* Utrecht, the Netherlands, VSP Science Press, 599–621.

——, M. Farrar, X. Xiang, and J. Turk, 1995b: Prospects for advanced radar–radiometer precipitation retrieval algorithms during the TRMM era. *Proc. Second Combined Optical-Microwave Earth and Atmosphere Sensing Symp.*, Atlanta, GA, IEEE/LEOS, 177.

Spencer, R. W., H. M. Goodman, and R. E. Hood, 1989: Precipitation retrieval over land and ocean with the SSM/I: Identification and characteristics of the scattering signal. *J. Atmos. Oceanic Technol.*, **6,** 254–273.

——, R. E. Hood, F. J. LaFontaine, E. A. Smith, J. Galliano, and E. Lobl, 1994: High-resolution imaging of rain systems with the Advanced Microwave Precipitation Radiometer. *J. Atmos. Oceanic Technol.*, **11,** 849–857.

Tanner, A., S. L. Durden, R. Denning, E. Im, F. K. Li, W. Ricketts, and W. Wilson, 1994: Pulse compression with very low sidelobes in an airborne rain mapping radar. *IEEE Trans. Geosci. Remote Sens.*, **32,** 211–213.

TCIPO Staff, 1993: TOGA COARE intensive observing period summary. TOGA COARE International Project Office. [Available from University Corporation for Atmospheric Research, P.O. Box 3000, Boulder, CO 80307-3000.]

Theon, J. S., T. Matsuno, T. Sakata, and N. Fugono, Eds., 1992: *The Global Role of Tropical Rainfall.* A. Deepak, 280 pp.

Turk, J., and J. Vivekanandan, 1995: Effects of hydrometeor shape and orientation upon passive microwave brightness temperature measurements. *Microwave Radiometry and Remote Sensing of the Environment,* D. Solimini, Ed., VSP Press, 187–196.

——, ——, F. S. Marzano, R. E. Hood, R. W. Spencer, and F. J. LaFontaine, 1994: Active and passive microwave remote sensing of precipitating storms during CaPE. Part I: Advanced Microwave Precipitation Radiometer and polarimetric radar measurements and models. *Meteor. Atmos. Phys.*, **54,** 3–27.

——, M. Farrar, E. A. Smith, and F. S. Marzano, 1995a: Measurements and implications for combined radar-passive microwave rainfall profiling techniques. *Proc. Second Combined Optical-Microwave Earth and Atmosphere Sensing Symp.*, Atlanta, GA, IEEE/LEOS, 183–185.

——, F. S. Marzano, A. Mugnai, and E. A. Smith, 1995b: Measure-

ments and applications for combined radar-passive microwave rainfall profiling during TOGA-COARE. *Proc. 1995 International Geoscience and Remote Sensing Symp. (IGARSS '95)*, Florence, Italy, IEEE/GRSS, 655–657.

——,——, E. A. Smith, M. R. Farrar, and A. Mugnai, 1995c: Radar and radiometeric measurements from TOGA-COARE: Application to a combined TRMM rainfall algorithm. Preprints, *27th Conf. on Radar Meteorology*, Vail, CO, Amer. Meteor. Soc., 786–788.

Ulbrich, C. W., 1983: Natural variations in the analytical form of the raindrop size distribution. *J. Climate Appl. Meteor.*, **22,** 1764–1775.

Vivekanandan, J., J. Turk, G. L. Stephens, and V. N. Bringi, 1990: Microwave radiative transfer studies using combined multiparameter radar and radiometer measurements during COHMEX. *J. Appl. Meteor.*, **29,** 561–585.

——, ——, and V. N. Bringi, 1993: Advanced Microwave Precipitation Radiometer (AMPR) and multiparameter radar comparisons of precipitation. *IEEE Trans. Geosci. Remote Sens.*, **31,** 860–870.

Webster, P. J., and R. Lukas, 1992. TOGA COARE: The Coupled Ocean–Atmosphere Response Experiment. *Bull. Amer. Meteor. Soc.*, **73,** 1377–1416.

Weinman, J. A., R. Meneghini, and K. Nakamura, 1990: Retrieval of precipitation profiles from airborne radar and passive radiometer measurements: Comparison with dual-frequency radar measurements. *J. Appl. Meteor.*, **29,** 981–993.

——, J. L. Schols, and L. S. Chiu, 1994: *Precipitation Distributions from Combined Airborne Microwave Radiometric/Radar Measurements and Ground Based VLF Sferics Observations in Support of NASA's Tropical Rainfall Measuring Mission*. NATO ASI Series, Vol. 126.

Wilheit, T. T., 1979: A model for the microwave emissivity of the ocean's surface as a function of wind speed. *IEEE Trans. Geosci. Remote Sens.*, **17,** 244–249.

——, 1995: TMI profiling algorithm. *TRMM Science Operations Plan*, J. Simson and C. Kummerow, Eds., NASA Goddard Space Flight Center, 15–16.

——, A. T. C. Chang, M. S. V. Rao, E. B. Rodgers, and J. S. Theon, 1977: A satellite technique for quantitatively mapping rainfall rates over the oceans. *J. Appl. Meteor.*, **16,** 551–560.

——, ——, and L. S. Chiu, 1991: Retrieval of monthly rainfall indexes from microwave radiometric measurements using probability distribution functions. *J. Atmos. Oceanic Technol.*, **8,** 118–136.

Xiang, X., E. A. Smith, and C. G. Justus, 1994: A rapid radiative transfer model for reflection of solar radiation. *J. Atmos. Sci.*, **51,** 1978–1988.

——, M. R. Farrar, and E. A. Smith, 1996: Combined radar–radiometer precipitation retrieval for TRMM. Part II: A unified RTE model for active and passive radiative transfer calculations. Preprints, *Eighth Conf. on Satellite Meteorology and Oceanography*, Atlanta, GA, Amer. Meteor. Soc., 266–267.

Yeh, H.-Y. M., N. Prasad, R. Meneghini, W.-K. Tao, J. A. Jones, and R. F. Adler, 1995: Cloud model–based simulation of spaceborne radar observations. *J. Appl. Meteor.*, **34,** 175–197.

Yuter, S. E., R. A. Houze Jr., B. F. Smull, F. D. Marks Jr., J. R Daugherty, and S. R. Brodzik, 1995: TOGA COARE aircraft mission summary images: An electronic atlas. *Bull. Amer. Meteor. Soc.*, **76,** 319–328.